1 Hyperspectral mapping of density, porosity, stiffness, and strength in

2 hydrothermally altered volcanic rocks

- 3 Samuel T. Thiele¹, Gabor Kereszturi², Michael J. Heap^{3,4}, Andréa de Lima Ribeiro¹, Akshay V. Kamath¹,
- 4 Maia Kidd², Matías Tramontini⁵, Marina Rosas-Carbajal⁶, Richard Gloaguen¹
- 6 ¹Helmholtz-Zentrum Dresden-Rossendorf, Helmholtz Institute Freiberg, Chemnitzer Str. 40, 09599 Freiberg, Germany
- 7 ²Volcanic Risk Solutions, School of Agriculture and Environment, Massey University, Palmerston North, New Zealand
- 8 ³Université de Strasbourg, CNRS, Institut Terre et Environnement de Strasbourg, UMR 7063, 5 rue Descartes, Strasbourg
- 9 F-67084, France
- 10 ⁴Institut Universitaire de France (IUF), Paris, France
- 11 ⁵CONICET Facultad de Ciencias Astronómicas y Geofísicas, Universidad Nacional de La Plata, Argentina
- 12 ⁶Université de Paris Cité, Institut de Physique du Globe de Paris, CNRS, F-75005 Paris, France
- **13** *Correspondence to*: Samuel T Thiele (s.thiele@hzdr.de)

14 Abstract. Heterogeneous structures and diverse volcanic, hydrothermal, and geomorphological processes hinder the 15 characterisation of the mechanical properties of volcanic rock masses. Laboratory experiments can provide accurate rock 16 property measurements, but are limited by sample scale and labor-intensive procedures. In this contribution, we expand on 17 previous research linking the hyperspectral fingerprints of rocks to their physical and mechanical properties. We acquired a 18 unique reflectance dataset covering the visible-near infrared (VNIR), shortwave infrared (SWIR), midwave infrared 19 (MWIR), and longwave infrared (LWIR) of rocks sampled on eight basaltic to andesitic volcanoes. We trained several 20 machine learning models to predict density, porosity, uniaxial compressive strength (UCS), and Young's modulus (E) from 21 the spectral data. Significantly, nonlinear techniques such as multilayer perceptron (MLP) models were able to explain up to 22 80% of the variance in density and porosity, and 65–70% of the variance in UCS and E. Shapley value analysis, a tool from 23 explainable AI, highlights the dominant contribution of VNIR-SWIR features that can be attributed to hydrothermal 24 alteration and MWIR-LWIR features sensitive to volcanic glass content and, likely, fabric and/or surface roughness. These 25 results demonstrate that hyperspectral imaging can serve as a robust proxy for rock physical and mechanical properties, 26 potentially offering an efficient, scalable method for characterising large areas of exposed volcanic rock. The integration of 27 these data with geomechanical models could enhance hazard assessment, infrastructure development, and resource utilisation 28 in volcanic regions.

30 1 Introduction

31 Society is dependent on subsurface resources, including groundwater (Foster et al., 2013), low-carbon energy (Lund and 32 Toth, 2021; Soltani et al., 2019) and critical raw materials (Lewicka et al., 2021). Simultaneously, population growth and 33 increasingly extreme weather (Aubry et al., 2022; Farquharson et al., 2015) expose a growing number of people to 34 geological hazards, including rock falls, landslides, and volcanic eruptions. Effective management of these resources and 35 hazards requires detailed characterisation of the subsurface geology, its physical properties (e.g., density and permeability). 36 and its mechanical behaviour (e.g., strength and deformability). 37 Volcanic regions commonly host mineral, water, and geothermal resources, and are also extremely prone to geological 38 hazards. However, the mechanical behavior of volcanic rock masses remains challenging to characterize, due to the diverse 39 volcanic, hydrothermal, sedimentological and geomorphological processes that shape and reshape them (Heap and Violay, 40 2021). Although mechanical properties can be accurately and routinely measured in the laboratory, samples are typically 41 limited to the centimeter- to decimeter-scale, which is several orders of magnitude smaller than is required to predict surface 42 deformation or reservoir behavior. Obtaining sufficient measurements to statistically characterize large-scale mechanical 43 variability thus remains a challenge, given the laborious mechanical tests required to measure e.g., strength, stiffness, and 44 hydraulic properties. 45 Several proxy measures have been developed to help mitigate sampling limitations, including field measurements of porosity 46 and permeability (Farquharson et al., 2015; Mordensky et al., 2018), Schmidt hardness (del Potro and Hürlimann, 2009; 47 Dincer et al., 2004; Harnett et al., 2019; Mordensky et al., 2018), point-load strength (Pogani et al., 2025), reflectance 48 spectroscopy (Kamath et al., 2025; Bakun-Mazor et al., 2024; Kereszturi et al., 2023; Schaefer et al., 2021), and thermal 49 inertia (Franzosi et al., 2023; Loche et al., 2021; Mineo and Pappalardo, 2016). These proxies are easier to obtain than many 50 mechanical test results, and often correlate well with important laboratory-measured properties like strength and stiffness 51 after calibration for specific geological contexts or settings. 52 Hyperspectral reflectance data could provide an especially useful proxy for mechanical properties, as they can be collected 53 rapidly and, potentially, acquired remotely using imaging sensors. This approach could make use of the latent influence that 54 lithological properties like mineralogy, fabric, and porosity have on both the hyperspectral and mechanical response. For 55 instance, Schaefer et al. (2021) used visible-near (VNIR; 350-900 nm) and shortwave (SWIR; 900-2500 nm) infrared 56 reflectance spectroscopy to correlate spectral features and mineralogy with porosity and strength, and identified moderate 57 Spearman rank correlation with 390, 2207, and 2325 nm features. Kereszturi et al. (2023) also used VNIR and SWIR 58 hyperspectral data to predict porosity and unconfined compressive strength (UCS) in volcanic rocks, explaining 40–50% of 59 the mechanical variance. Lee et al. (2023) applied VNIR, SWIR, and midwave infrared (MWIR; 3000-5200 nm) data to 60 predict the dynamic elastic moduli of finely laminated shales, with R² scores between 0.4 and 0.8, but across a small sample 61 set. Most recently, Bakun-Mazor et al. (2024) used VNIR-SWIR and longwave infrared (LWIR; 7000–12000 nm) spectra to 62 estimate several mechanical properties, including UCS, in carbonate rocks, with generally high (0.8 to 0.9) R² scores.

- 63 However, further research is needed to understand the relationships between hyperspectral data and the mechanical 64 properties of volcanic rocks, due to their complex microstructures and mineralogies, as well as the impact of hydrothermal 65 alteration.
- 66 In this contribution we investigate the relationships between hyperspectral data and the mechanical properties of volcanic
- 67 rocks, specifically focusing on density, porosity, UCS, and Young's modulus (E). E is of particular interest, as it has not
- 68 previously been linked to hyperspectral data and is crucial to predict surface deformation occurring during e.g. construction
- 69 or tunnelling works, mining, and volcanic unrest (Arens et al., 2022; Harnett and Heap, 2021; Heap et al., 2020b, 2021b;
- 70 Hickey et al., 2022; Hoek and Diederichs, 2006; Strehlow et al., 2015; Vrakas et al., 2018).
- 71 We therefore expanded the dataset presented by Kereszturi et al. (2023) to include samples from more volcanoes, and cover
- 72 an extended spectral range (VNIR-SWIR-MWIR-LWIR). This dataset is then leveraged to:
- 1. Train machine learning models to predict density, porosity, UCS, and E.
- 74 2. Identify hyperspectral indicators for hydrothermal alteration, and explore how these are linked to the measured and predicted mechanical properties.
- 76 3. Quantify the influence of different spectral ranges on each predicted property, to explore the spectral features that inform our model.
- 78 By advancing our understanding of the correlations between hyperspectral and mechanical properties, we ultimately aim to 79 improve our ability to characterise complex and heterogeneous volcanic rock masses.

802 Theory

81 2.1 Light-matter interactions: reflection and scattering

- 82 Light-matter interactions are complex, and governed by multiple interacting optical phenomena. Reflectance is a
- 83 dimensionless expression of these interactions, defined by the ratio between the excitation signal (illumination or irradiance,
- 84 W.m-2) and signals emitted back towards a sensor (radiance, W.m-2.sr-1). Hyperspectral sensors measure this returned
- 85 radiance, and split it into many narrow but contiguous wavelength ranges to derive a radiance spectra that, after correction to
- 86 derive reflectance, contains information on the target material.
- 87 Links between hyperspectral reflectance spectra and mineralogy are well established, as reviewed by Laukamp et al. (2021)
- 88 and Williams and Ramsey (2024). Specific spectral ranges can be used to identify certain elements, due to the absorption of
- 89 VNIR range light during electronic transitions in metals like Fe, and covalent bonds that absorb energy at specific
- 90 wavelengths by stretching and bending activity. Compounds containing O-H, C-O and S-O bonds tend to have diagnostic
- 91 absorption features in the SWIR and MWIR ranges, while stretching and bending vibrations of Si-O bonds cause absorption
- 92 in the upper MWIR and LWIR ranges.
- 93 In volcanic contexts, electronic transition absorptions in the VNIR range can be used to detect common Fe3+ and Fe2+ rich
- 94 minerals, including hematite, goethite, and jarosite. SWIR range data are sensitive to hydroxylated silicates, including clay

95 minerals, sulphates, and carbonates. The MWIR range is less widely used, but also includes diagnostic absorption features 96 for hydroxylate silicate and carbonate minerals. Finally, the upper MWIR and LWIR range is strongly influenced by 97 absorptions from the Si-O bonds in silicate minerals and glasses, and can be used to characterise the extent of silica 98 polymerization and to identify most rock-forming silicates (e.g., quartz, feldspars, pyroxene).

99 Regardless of the spectral range, features observed in reflectance spectra are determined by a combination of refraction, 100 absorption and scattering characteristics inherent to each material, and abide by Snell's law (Kirkland et al., 2003; Rost et al., 101 2018). The expected positions of absorption features are well-established, including subtle variations caused by differences 102 in crystal structure that often allow precise identification of specific minerals (Laukamp et al., 2021). However, spectral 103 characteristics like overall albedo, broad fluctuations in reflectance intensity, and the depth and asymmetry of absorption 104 modes (spectral contrast), can vary significantly between rocks with the same mineralogy. These wavelength-dependent 105 variations derive from processes occurring as light interacts with the surface of a rock and while traveling through its solid 106 constituents (and pore spaces), carrying information linked to surface and bulk physical properties. For consistency, we refer 107 to changes in the direction and intensity of light which are directly dependent on the surface characteristics as 'surface 108 scattering', and as 'volume scattering' when these changes are linked to processes occurring below the surface. Accordingly, 109 light-matter interactions in natural minerals can be understood through the combination of two optical scattering 110 components: surface and volume (Osterloo et al., 2012; Rost et al., 2018; Vincent and Hunt, 1968).

111Surface scattering occurs when light interacts mostly with the superficial layer of a mineral, which acts as a mirror-like 112 interface and reflects light without transmitting it to the internal constituents of a rock (hereafter referred to as grains, 113 although we use this term inclusively of crystals, clasts and fragments) (Fig. 1a). This happens when the extinction 114 coefficient of light in a medium (k) is larger than its refractive index (n); as most of the incident radiation is absorbed at the 115 surface and not transmitted to higher depths (Hardgrove et al., 2016). The magnitude of surface scattering can vary with 116 wavelength (as n and k are both wavelength dependent), and is highly sensitive to the scale of surface topography relative to 117 the wavelength (Rayleigh's criterion; Hapke, 2012, 1981). A surface is considered perfectly smooth when its average 118 roughness is smaller than the wavelength of the incident light, with the outcoming light being reflected at the same angle as 119 the incoming radiation. This phenomenon, known as *specular reflection*, is particularly important in the LWIR region 120 (5,000–50,000 nm) (Fig. 1a). As roughness increases, surface irregularities serve as points for the incoming light to scatter 121 into several directions, spreading the total reflected energy in a Lambertian-like process known as *diffuse scattering* (Fig. 122 1a). Diffuse scattering is particularly important in the VNIR-SWIR analysis of rough surfaces in which asperities are 123 oriented towards different directions. In extreme cases, multiple diffuse patterns can occur within a small area, leading to a 124 multi-path scattering pattern (Fig. 1a).

125 In addition to impacting surface scattering, increased roughness enhances the transmission of incoming light through grains 126 at the sample surface, even when k is larger than n. This process, known as *volume scattering*, introduces longer paths and 127 changes in direction for light travelling within the medium leading to partial energy loss and reduced spectral contrast 128 (Kirkland et al., 2003, 2001; Osterloo et al., 2012; Rost et al., 2018) due to light undergoing absorption within the medium

129 prior to being scattered back to the surface (Fig. 1d). Increased volume scattering is also linked to the grain size, and 130 observed especially in the presence of smaller grains (Hunt and Vincent, 1968; Lyon, 1965; Mustard and Hays, 1997; 131 Salisbury and Wald, 1992). It is important to note that although the impact of volume scattering on the reflectance spectrum 132 is dependent on the inherent optical properties of the mineral, roughness, and the wavelength of the incoming light, these 133 relationships are highly non-linear and difficult to characterise for real multi-phase materials (i.e. rocks). In the LWIR, both 134 increased and decreased spectral contrast have been associated with volume scattering, highlighting the complexity of these 135 interactions (Osterloo et al., 2012).

136 For most real materials and mineral mixtures, both surface and volume scattering influence the reflectance spectra, with 137 different contributions depending (again) on the surface roughness, grain size, and wavelength range. An exemplary case of 138 surface and volume processes acting simultaneously is encountered for porous materials (Fig 1e). Pore size, shape and 139 distribution are directly linked to surface roughness, impacting the light-matter interaction dynamics by: i) enhancing the 140 volume scattering by transmitting light through regions with different *k* and *n* (e.g. mineral/air/mineral interfaces), leading to 141 longer travel paths; and ii) by trapping light at pores with high depth-to-width ratios, causing multiple surface reflection 142 paths (cavity effect) and, in extreme cases, leading to total absorption of light before it can be reflected out of the cavity 143 (Hardgrove et al., 2016; Huang et al., 2021; Kirkland et al., 2001). Ultimately, increased porosity may lead to important 144 changes in the reflectance spectrum, particularly in the thermal region (5,000–50,000), and is associated with reduced 145 spectral contrast and inhibition of diagnostic mineralogical absorption features (Osterloo et al., 2012; Rost et al., 2018; 146 Salisbury and Eastes, 1985).

1472.2 Hapke's model

148 Hyperspectral cameras operate as fixed-position external-reflectance sensors, collecting the radiation scattered in a specific 149 direction from a material excited by a light source of known characteristics. Hence, material properties which affect the 150 amount of radiation scattered towards a detector influence the measured spectra. Several models (broadly known as the 151 Hapke model) have been proposed to investigate these light-mineral interaction dynamics, initially in the context of 152 extraterrestrial remote sensing (Hapke, 2012, 2008, 2002, 1984, 1981). Hapke's models aim to estimate bidirectional 153 reflectance signals collected by external-reflectance sensors. They are based on radiative transfer theory and on the works 154 from Chandrasekhar (1960), and form an important theoretical basis for hyperspectral imaging applications. The core 155 premise of Hapke's models is that reflectance spectra can be parameterised as a function of material type and morphological 156 properties (Hapke, 1993).

157 While a detailed examination of Hapke's model(s) is beyond the scope of this contribution, we aim here to identify several 158 key elements that link reflectance signals with roughness, grain size and porosity. These effects are highlighted using the 159 following formula,

160
$$r(i, e, \alpha, \lambda) = K \frac{\omega(\lambda)}{4} \left([1 + B(\alpha)] P(\alpha) + M(i, e, \alpha, \lambda) - 1 \right), \tag{Eq. 1},$$

162 where $r(i,e,\alpha,\lambda)$ is the scattering intensity (radiance); K is the filling factor (linked to porosity; Hapke, 2008); ω (λ) is the 163 average single scattering albedo (SSA; linked to absorption and scattering at particle level and dependent on the wavelength 164 λ); $B(\alpha)$ is the opposition surge function (Hapke, 1993, 1986); $P(\alpha)$ is the average single scattering function for the phase 165 angle α ; i and e are the angles of incidence and emission; $M(i,e,\alpha,\lambda)$ represents the wavelength-dependent multiple scattering 166 effect (MSE). It is important to note that Hapke's refers to 'scattering' as an integration of all radiation emitted by a surface 167 following interactions with an excitation source, with no distinction between surface and volume processes. Instead, the 168 models provide a holistic approach in which multiple terms are influenced by both surface and volume processes. In this 169 context, radiance is thus the total signal scattered by an object towards a detector. In hyperspectral remote sensing, the 170 distinction between surface and volume scattering contributions is important, as surface and subsurface rock characteristics 171 are linked to changes in the reflectance spectra (cf., section 2.1).

173 The single and multiple scattering terms (SSA and MSE) are the primary contributors to the reflectance estimated by the 174 model. Whilst SSA represents the probability of light being scattered or absorbed by a single grain, MSE (derived from 175 Ambartsumian-Chandrasekhar H-function and dependent on SSA) accounts for multiple scattering prior to its emission 176 towards a detector. Both parameters are material-specific, and vary according to changes in roughness, grain size, and 177 wavelength of light. Another core term is the phase function $P(\alpha)$, which estimates how much light is scattered in a given 178 direction relative to the direction of incoming light as a function of the angle between the illumination direction and the 179 viewing direction (phase angle, α). The intensity and direction of the phase function are not material-specific, but α also 180 depends on roughness, grain size and wavelength. The opposition surge term $B(\alpha)$ is also linked to α , and introduces a 181 surface brightening effect as it decreases (Hapke, 2002). Finally, the porosity parameter K accounts for changes in scattered 182 signals due to increasing porosity and/or decreasing density (Hapke, 2008).

184 To summarise, Hapke's models provide an important tool to understand the link between hyperspectral reflectance spectra 185 and sample roughness, grain size, porosity and composition. It is based on radiative transfer theory and traditionally used to 186 describe the scattering of light by planetary surfaces. It estimates the bidirectional reflectance of a surface, considering both 187 single and multiple scattering of light. The model can be tuned for specific applications, and generally incorporates 188 parameters such as single-scattering albedo, phase function, and surface roughness which have a direct impact on the 189 bidirectional reflectance signals. Hapke's model is therefore a strong basis for understanding the interaction of light with rock 190 surfaces, aiding in the interpretation of remote sensing data. While the complexity of real samples typically limits the 191 model's practical application, it provides a useful theoretical framework that will help us to understand and interpret 192 hyperspectral reflectance spectra.

1943 Methods

1953.1 Sample database

196 For this study, we compiled a new database of 332 well-characterised core samples that have been subjected to laboratory 197 rock deformation experiments (Heap et al., 2021a, 2020a; Leiter et al., 2024; Schaefer et al., 2023; Tramontini et al., 2025; 198 Vairé et al., 2024). These samples were collected in the scope of previous studies from eight basaltic to rhyolitic composite 199 volcanoes, including Cracked Mountain (Canada; Leiter et al., 2024), Ruapehu (New Zealand; Schaefer et al., 2023), La 200 Soufrière de Guadeloupe (Eastern Caribbean; Heap et al., 2021b, 2021a), Ohakuri (New Zealand; Heap et al., 2020a), 201 Chaîne des Puys (France; Vairé et al., 2024), Copahue (Argentina/Chile; Tramontini et al., 2025), Tongariro (New Zealand; 202 Kidd et al., 2025), and Whakaari (New Zealand; Kidd et al., 2025).
203 Most of the sampled rocks are basaltic to andesitic in composition, and cover a range of textures (breccias, pyroclastic, and 204 coherent lava rocks). A breadth of hydrothermal alteration is also covered, ranging from dominantly fresh rocks (e.g., from 205 Chaîne des Puys; Vairé et al., 2024) through to intense hydrothermal alteration (e.g., some samples from Ruapehu and 206 Whakaari; Schaefer et al., 2023). Altered samples in our sample set were subject to acid-sulphate related mineralogical 207 changes, including the formation of sulphates (e.g., jarosite, alunite and anhydrite), phyllosilicates (e.g., kaolinite and 208 montmorillonite), and various polymorphs of quartz (Heap et al., 2021a; Kereszturi et al., 2020). This diversity of alteration 209 is intended to help our machine learning models to learn some of the alteration systematics and capture how these can 210 influence the physical and mechanical properties of volcanic rocks.

2113.2 Laboratory testing

212 Mechanical test cores were prepared with a diameter of 20 mm and a length of ca. 40 mm. Measurements and experiments 213 were either performed at University of Strasbourg (France) or University of Canterbury (New Zealand). Prior to testing, the 214 samples were dried in a vacuum oven at 40 °C for a minimum of 48 hours (Strasbourg) or oven-dried at 60 °C for a 215 minimum of 48 hours (Canterbury). Dry bulk density was calculated using the dry mass and bulk volume of each sample. 216 Connected porosity was calculated using the skeletal volume, measured using an AccuPyc II 1340 pycnometer (Strasbourg 217 and Canterbury), and the bulk volume of each sample. 218 Uniaxial compressive strength (UCS) experiments were performed using a uniaxial load frame supplied by Schenk 219 (Strasbourg) or a 3000 kN Technotest uniaxial load frame (Canterbury). All experiments were performed on dry samples at 220 ambient laboratory temperatures. Samples were deformed at a constant strain rate of 10–5 s–1 until macroscopic sample 221 failure (Fig. 2a). Axial displacement and axial force were measured by a linear variable differential transducer and a load 222 cell, respectively, and were converted to axial strain and axial stress using the initial length and radius of the sample, 223 respectively. More information, as well as schematic diagrams of the devices, can be found in Heap et al. (2014) and 224 Mordensky et al. (2018).

225 First, the maximum stress of each loading curve was identified as the UCS. The pre-failure loading curve was then smoothed 226 slightly using a Savitzky–Golay filter and resampled to regular stress increments using a linear interpolation. The slope of 227 the most linear part of the resampled loading curve was then identified to calculate E, using the random sample and 228 consensus (RANSAC) algorithm. This regression technique robust to outliers iteratively fits data with a function (in this case 229 linear) using random minimal subsets (two points) and maximises the number of inliers within a threshold distance. This 230 approach successfully identifies the linear part of each loading curve while remaining robust to outliers caused by pre-failure 231 inelastic deformation by maximising the number of inliers (rather than minimising residuals as per e.g., least-squares 232 regression, Fig. 2c), allowing robust and objective measurement of E.

2333.3 Hyperspectral data acquisition

234 The core samples were arranged on non-reflective sample trays (Fig. 2a), grouped by size to limit focal blur, leveled and 235 fixed in place using plasticine to reduce illumination artifacts. Each tray was then scanned using a Specim SiSuROCK drill 236 core scanner, which contains Specim AisaFENIX, FX50 and AisaOWL hyperspectral sensors and a high spatial Specim 237 RGB-Jai camera (Fig. 2b). The workflow described by Thiele et al. (2024) was used to coregister data from each of the 238 sensors and to convert from measured radiance to relative reflectance.

239 Each sample was then extracted from the coregistered stack of hyperspectral (and RGB) imagery using napari-hippo (Thiele 240 et al., 2024), and stored as a separate set of images. The spectra of each image was smoothed slightly with a Savitzky–Golay 241 filter (using a 1st order polynomial and window size of 5 bands), and hull-corrected using hylite (Thiele et al., 2021) to 242 amplify spectral absorption features and reduce illumination artifacts caused by non-planar sample geometries. VNIR to 243 MWIR spectra were corrected using an upper hull correction, while a lower hull correction was applied to the LWIR range 244 data.

245 Median spectra from each mechanical test sample were then compiled into a spectral library covering the 246 VNIR-SWIR-MWIR-LWIR range. These were combined with the corresponding mechanical property measurements to 247 derive a training dataset.

248 Their mineralogy was characterised by indices extracted from the spectra of each sample using the minimum wavelength 249 mapping approach (van der Meer et al., 2018) implemented in hylite (Thiele et al., 2021). These indices (Table 1) quantify 250 specific spectral absorptions resulting from vibrational and bending vibrations associated with water, sulfate, hydroxylated 251 phyllosilicates, and silicate minerals (Laukamp et al., 2021; Schodlok et al., 2016). Two composite indices were also 252 calculated, to characterize bulk-composition and the extent of hydrothermal alteration. The first is the Mafic-Felsic Index of 253 Schodlok et al., (2016), which distinguishes samples with basaltic compositions from those that are more evolved. This 254 index, hereafter referred to as MFI, was computed by applying a lower-hull correction to the LWIR spectra between 7640 255 and 10620 nm and identifying the general position (wavelength) of the reflection peak within this range, using the 256 polynomial fitting approach implemented in hylite (Thiele et al., 2021). The results were then normalized to range between 0 257 (maxima at 10620 nm, indicating mafic compositions) and 1 (maxima at 7640 nm, indicating felsic compositions).

258 The second bulk index was derived by averaging the H2O and OH absorptions at ~1900 and 1400 nm (Table 1), to track the 259 total amount of water (as H2O, in e.g. quartz-hosted fluid inclusions, and as -OH groups in e.g., clay minerals). Because 260 most of the measured volcanic rocks are initially dry (with some exceptions, e.g., phreatomagmatic tuff), this water often 261 indicates hydrothermal alteration. We thus use this index as a rough proxy for hydrothermal alteration (and weathering) 262 processes. The presence of hydrated (alteration) minerals has been shown to correlate with mechanical response (Heap et al., 263 2022).

264

2653.4 Regression models

267 and ensure the back-transformed predictions are correctly scaled (non-negative and, in the case of porosity, between 0 and 1).
268 A square root transform (Fig. 3e) was found to perform better than a log-transform (Fig. 3f), likely as it resulted in more
269 normally distributed data. Porosity was converted to a ratio of voids to solids (1 - porosity) prior to the square root transform,
270 mitigating challenges fitting regressions to closed data.
271 We ensure a robust calibration/validation by defining five folds using a stratified split with respect to porosity, to ensure that
272 each fold contains diverse mechanical properties. Several machine learning approaches (lasso regression, partial least square
273 regression, support vector regression, and multilayer perceptron regression), known to be adapted to this genre of tasks,
274 were then evaluated using the R2 metric and 5-fold cross validation (to account for potential overfitting). Model
275 hyperparameters were optimised to maximise the training R2 score, as documented in the Jupyter notebooks included in the
276 supplementary material. Five models of each type were trained, each setting aside a single fold (20% of the data) as a test set.

266 Each target variable (density, porosity, UCS, and E) requires transformation prior to model fitting, to reduce skew (Fig. 3)

277 Each trained model was then used to predict its unseen test-set, and the results compiled for a robust assessment of model

278 accuracy. Finally, the best performing models (of different types) were combined into an ensemble, allowing prediction

279 variance to be used as a measure of uncertainty.

2803.5 SHAP analysis

281 Shapley values (Shapley, 1973) have recently been adapted to help understand the predictions made by deep learning 282 models. Based on cooperative game theory, Shapley values quantify the contribution of individual features to output 283 predictions, providing a theoretically grounded measure of the average marginal contribution of each input feature across all 284 possible feature subsets (Lundberg and Lee, 2017). This allows a more detailed interpretation than other explanation 285 approaches, and in this case helps link model predictions to specific hyperspectral bands.

286 We used the python package SHAP (Shapley Additive Explanations; Lundberg and Lee, 2017) to compute Shapley values 287 for our ensemble models. Due to the various types of models included in these ensembles, a stochastic estimation approach 288 (KernelSHAP) was used. KernelSHAP is a model-agnostic algorithm that estimates Shapley values by systematically 289 perturbing input variables and measuring the resulting changes. The perturbative nature of this algorithm makes it

290 computationally expensive, requiring us to compute Shapley values only for a subset of our test dataset. This subset was 291 selected using k-means clustering, such that 16 representative data points (cluster centroids) could be selected for use by the 292 Kernel Explainer.

2934 Results

294 4.1 Spectral response of hydrothermal alteration

295 A comparison of MFI, a proxy for composition, and hydration index, a proxy for hydrothermal alteration, highlights the 296 spectral diversity of our dataset (Fig. 4). Two broad populations of basalt (lower) and andesite (upper) form clear horizontal 297 "bands", each of which contains variable amounts of hydration. The MFI results broadly match the expected composition of 298 each volcano, albeit with exceptions including two altered samples from Whakaari with anomalously low MFI (due to the 299 confounding influence of non-silicate alteration minerals like jarosite or sulphur, rather than a mafic composition). 300 Diagnostic absorption features for kaolinite ($v+\delta M2OHo$) and other clay minerals ($v+\delta (A1)-OH$ and $v+\delta (Mg)-OH$) are 301 prominent in many altered samples. Of these, the kaolinite-rich samples (Fig. 4e) tended to be associated with deeper 2vSi-O 302 absorptions in the MWIR range (at ~4500 nm and indicative of silicification) or δS-O absorptions in the SWIR range (at 303~1750 nm), indicating silicification and/or the presence of sulphate minerals like jarosite and alunite. In combination, these 304 spectral features indicate advanced argillic alteration, and are mostly associated with higher (andesitic) values of MFI (as our 305 dataset currently lacks basaltic examples of advanced argillic alteration). 306 Many samples also contain well defined $v+\delta(Al)$ -OH absorption features (Fig. 4a), but without the previously mentioned 307 kaolinite, sulphate, or quartz-related absorption features. These are indicative of illite and smectite group clay minerals 308 formed by lower-temperature (<120° C) and/or higher pH hydrothermal alteration or weathering. Many of the basaltic 309 samples (lower MFI) also contain distinctive v+ δ (Mg)OH absorption features at 2300 nm, while lacking the v+ δ (Al)-OH 310 feature (Fig. 4b). We interpret this as either primary Al-poor clays (e.g., in palagonite tuffs), or as the result of argillic 311 alteration or weathering in Al-poor primary lithologies to form Fe- and Mg- rich clay minerals, like nontronite and hectorite. 312 Notably, all samples with spectral absorptions indicative of hydrothermal alteration also had prominent vOH and 313 vOH+δH2O absorptions at ~1400 and 1900 nm. This suggests that these combined features (our hydration index) can be 314 used to broadly quantify the intensity of hydrothermal alteration, because primary volcanic lithologies tend not to contain 315 hydrated or hydroxylated phases. Samples with higher hydration indices tended to be less dense (Fig. 5a) and have lower 316 UCS and E (Fig. 5c-d) than counterparts with lower hydration indices. Porosity showed a more complex relationship to the 317 hydration index (Fig. 5b), with a distinctive set of highly porous but non-hydrated samples (vesiculated lavas), and highly 318 porous and hydrated samples.

3194.2 Rock property prediction

320 The tested machine learning models gave a wide range of prediction accuracies, with highly varied 5-fold cross-validation 321 R2 scores (Table 2). Linear models (PLSR and Lasso) performed poorly, suggesting a highly non-linear relationship between 322 spectral response and rock properties (Table 2). Support Vector Regression (SVR) and Multilayer Perceptron (MLP) models 323 were able to learn the nonlinear relations, yielding 5-fold cross validated R2 scores between 0.5 and 0.85 for each of the rock 324 properties. Deeper multilayer perceptrons (with 8 to 16 fully connected layers) performed best. The need for depth further 325 emphasises the need to capture nonlinear links in the underlying data structure and modelling.

326 Models fit to principal component (PCA) transformed inputs (retaining 25 independent features), including the MLP models 327 that theoretically work well with high-dimensionality input, performed better than models fit directly to concatenated 328 spectra.

329 No substantial difference in accuracy was observed between MLP models predicting a single output (i.e. univariate MLP 330 models that predict a single rock property) and multivariate MLP models (that predict each of the four rock properties 331 together). Ensemble predictions computed by averaging outputs from a set of nine manually selected (best-performing) SVM 332 and MLP models show similar or slightly improved R2 scores (relative to the individual models). However, these ensemble 333 models allow an estimate of prediction uncertainty (Fig. 6), based on the standard deviation (σ) of the individual model 334 predictions. In most cases the measured rock property was within 2σ of the ensemble mean, though several notable outliers 335 can also be identified. These include the prominently under-predicted UCS for one sample from Ruapehu (156 rather than 336 380 MPa), and over-estimated E for several samples from Ruapehu and Whakaari.

337 Interestingly, models trained and tested on the basaltic samples achieved higher R2 scores than equivalents trained and tested 338 on andesitic ones (Table 2). This implies that the rock properties of basalts (in our dataset) were easier to predict than 339 andesites, possibly due to the variability of the hydrothermally altered andesite relative to the basalts (which were mostly 340 fresh or palagonitized).

341 4.3 Important spectral ranges

342 Shapley values calculated for our ensemble predictions were aggregated to explore the contribution of each spectral range.
343 This result exploits the additive nature of Shapley values: values derived for bands in the VNIR, SWIR, MWIR and LWIR
344 ranges (respectively) can be summed to quantify the aggregate effect of each spectral range on each model prediction (Fig.
3457). The results suggest the VNIR-SWIR range contributes most to predictions of density, UCS, and E that are below the
346 expected (average) prediction, while the LWIR range makes a substantial contribution for above-average predictions. The
347 opposite can be seen for porosity, where VNIR-SWIR bands mostly drive above average predictions. This pattern suggests
348 the models learn to associate SWIR-active alteration minerals with reduced UCS, E, and density (and increased porosity).
349 The non-aggregated (per-band) Shapley values can also constrain the specific spectral features that, in combination,
350 contribute to increase or decrease each prediction relative to the mean. These values are shown in Fig. 8, though only for

351 models trained on the basaltic (Fig. 8a) and andesitic (Fig. 8c) subsets separately (to reduce the influence of lithological 352 effects). The results are difficult to interpret specifically because the predictions result from a complex balance between 353 positive contributions from some bands (red) and negative contributions (blue) from others. Strongly negative Shapley 354 values are often associated with 1800, 1900, and 2200 nm bands, which contain absorptions characteristic of hydrothermal 355 alteration minerals (Table 1) for samples with low predicted E. Higher predictions also appear driven by these same bands, 356 possibly due to an absence of absorption features in these wavelengths for these samples. In the MWIR, features at ~3400 357 and between 4200 and 4900 nm appear important, with several "doublets" (spectrally adjacent high and low Shapley values) 358 indicating a sensitivity to absorption shape (asymmetry) or position. The first of these bands (3400 nm) is likely related to 359 v2HOH absorptions (though this absorption will have been heavily distorted by the hull correction applied during 360 pre-processing). The latter bands (4200–4900) are interpreted to relate to 2vSi-O absorptions from silicate minerals or 2vS-O 361 absorptions from sulphates (Laukamp et al., 2021). The last of these (4900) may also have been shifted by the hull 362 correction.

363 The Shapley values are easier to interpret after averaging their absolute value across all samples, to broadly highlight 364 important spectral ranges. As mentioned also above, these ranges (Fig. 8b and Fig. 8d) match several expected mineralogical 365 absorptions but, interestingly, also suggest that the model tends to focus on absorption "shoulders" rather than their centres, 366 which we speculate could be due to a higher sensitivity of absorption shoulders to complex scattering effects.

367 Notably, many more VNIR, SWIR, and MWIR bands appear important for predictions made by the andesitic model than the 368 basaltic one, presumably due to the more complex mineralogy of these samples. Informative bands in the LWIR range 369 between 8500 and 11000 nm and also likely relate to vSiO absorptions, though the mixtures of silicate minerals and glassy 370 matrix make these difficult to interpret specifically (Laukamp et al., 2021; Leight et al., 2024; Williams and Ramsey, 2024). 371 Informative bands for the andesite model are lower wavelength (8500–9200 nm) than those for the basaltic model 372 (8800–9800 nm), corroborating the change in silica polymerization between these sample sets.

3735 Discussion

374 Our five-fold cross validated ensemble predictions show that hyperspectral data can be used to explain ~80% of the variance 375 in density and porosity and 65–70% of the variance in strength (UCS) and Young's modulus (E), at least for the investigated 376 basaltic and andesitic volcanic lithologies. The rapid acquisition and imaging abilities of hyperspectral sensors could thus be 377 leveraged to better characterise complex volcanic rock masses, by extending laborious rock property measurements across 378 large datasets from point spectrometers, hyperspectral core scanners and, potentially, outcrop hyperclouds (e.g., Thiele et al., 379 2024, 2022). The resulting thousands to millions of (ideally spatially continuous) property estimates would allow robust 380 characterisation of the variability in volcanic rock matrix properties and, if combined with digitally mapped fracture 381 information, provide some of the information needed to numerically predict larger-scale rock-mass properties (e.g., Cundall 382 et al., 2008).

383 5.1 Predicting density and porosity

384 Our predictions of density and porosity were remarkably accurate (5-fold CV R2 score of 0.81 and 0.84 respectively), 385 especially given the complex volcanic processes that influence these properties (vesiculation, pyroclastic processes, 386 alteration, and fracturing). Interestingly, linear methods such as LASSO and PLSR predicted density and porosity poorly 387 (Table 2), while the non-linear methods (MLP and SVR) achieved R2 scores >0.8. This suggests an inherently non-linear 388 relationship between reflectance, density, and porosity. The high accuracies of the non-linear models also indicate that they 389 are able to learn more than just the link between the hyperspectral data and mineralogy, as composition alone is expected to 390 be a poor predictor of porosity (Pola et al., 2012). We thus suggest that the hyperspectral data contain information on 391 porosity and density via the sensitivity of volume and surface scattering processes to pores at or near the sample's surface 392 (Fig. 1). As described by the Hapke model, such wavelength-dependent scattering effects are likely especially relevant for 393 longer wavelengths, supporting the Shapley values that show the LWIR data contributed significantly to many predictions 394 (Fig. 7). Larger vesicles that approach the 1 to 2 mm spatial resolution of the sensors could also influence the spectra, via the 395 cavity effect (Fig. 1), especially in the LWIR infrared range (where they are expected to reduce reflectivity and increase the 396 emissivity).

397 Our Shapley values highlight the important role of MWIR and LWIR bands, especially for high-density and low-porosity 398 samples (Fig. 7). It is also striking that the VNIR-SWIR and LWIR ranges tend to be in opposition (cancelling each other 399 out) for less extreme predictions (Fig. 7), emphasising the importance of the broad spectral range 400 (VNIR-SWIR-MWIR-LWIR) covered by the dataset. The special attention our machine learning models appear to be giving 401 to the shoulders of mineralogical absorption features (rather than their minima, which are typically related to composition) is 402 also noteworthy. We tentatively suggest that this highlights the sensitivity of our models to the shape and asymmetry of 403 absorption features, properties that are more significantly influenced by surface reflection and volume scattering processes 404 that likely give crucial information on surface roughness, grain size, and porosity.

405 5.2 Predicting uniaxial compressive strength and Young's modulus

406 The lower, but still informative, predictive power of our models for UCS and E indicates a complex relationship between 407 spectral response, porosity, density, and alteration-related weakening (Heap et al., 2020a, or possibly strengthening in the 408 case of silicification; Heap et al., 2021a). These non-linear models can explain \sim 70% of the total variance, noting that the R2 409 scores are likely substantially reduced by a small number of outliers (Fig. 6). This result is consistent with the combined 410 models of Kereszturi et al. (2023), in which externally measured porosity and VNIR-SWIR information (characterising 411 alteration mineralogy) explained 80% of the variance in UCS. We suggest that externally measured porosity was needed by 412 Kereszturi et al. (2023) due the lack of LWIR information, which limited their ability to directly predict porosity from the 413 hyperspectral data (R2 = 0.4). Our dataset clearly did not have this limitation (Section 5.1), indirectly improving also our 414 predictions of UCS.

415 Theoretical links between reflectance spectra and grain size properties could further influence our machine learning models, 416 although we are unable to distinguish these effects from the previously discussed sensitivity to porosity. We also speculate 417 that it is likely the model is learning to distinguish glass-rich (and hence stiff and brittle) samples from more crystallised 418 ones, based on their distinctive LWIR expression (Williams and Ramsey, 2024). The sensitivity to glass could explain the 419 broad informative wavelength range indicated by the Shapley values in the LWIR (Fig. 8).

420 The remaining (unpredicted) variance in UCS and E could be attributed to micro-fractures, which will serve to reduce E and

421 UCS (Griffiths et al., 2017; Swanson et al., 2020; Takemura et al., 2003) with negligible spectral effect. Such fractures could, 422 for example, explain overpredicted outliers in Figs. 6 and 8. Micro-fractures are less likely to explain cases where our model 423 makes under-predictions however, including the notable outlier in Fig. 6c where the predicted UCS is ~250 MPa too low.

425 VNIR-SWIR hyperspectral data are particularly useful for identifying hydrothermal alteration, discriminating between

424 5.3 Hyperspectral quantification of hydrothermal alteration

426 different alteration types, and vectoring towards mineral deposits (e.g., Cudahy et al., 2008; Laukamp et al., 2021, 2011; 427 Portela et al., 2021). Argillic and advanced argillic alteration can be characterised based on the distinctive spectral signature 428 of sulphates, kaolinite, and other clay minerals (Fig. 4). This could be further refined by detailed investigation of the position 429 of these respective absorption features, to distinguish between e.g., kaolinite and dickite or illite and smectite (e.g., 430 Kereszturi et al., 2020; Simpson and Rae, 2018).

431 Our results also show that the combined depth of v-OH and v+δH-O-H absorptions can be used as a broad but useful proxy 432 for hydrothermal alteration in non-weathered crystallised volcanic rocks, as these lithologies tend to be initially water poor. 433 That said, this index likely cannot identify hydrothermal alteration in tuff units, which can be hydrated during or shortly after 434 formation (e.g., palagonite). Our hydration index shows a weak correlation with physical and mechanical properties (Fig. 5), 435 with substantial unexplained variance that emphasises the important additional influence of microstructure (porosity, 436 grain-size, glass content, and micro-fractures).

437 5.4 Applications and future directions

438 Unlike other commonly applied proxies for physical and mechanical rock properties (e.g., Schmidt hardness, field estimates 439 for porosity, etc.), hyperspectral data can be collected remotely using imaging techniques. This imaging capability unlocks 440 several intriguing possibilities.

441 Firstly, our machine learning models could be applied to hyperspectral imagery of hand-sample sized specimens acquired 442 during geotechnical fieldwork to create prior predictions of their physical and mechanical property variability. The locations 443 of extracted mechanical test cores could then be optimized to cover the range of expected variability, improving the 444 statistical representativity of the resulting data. Such an approach would provide an opportunity to independently validate our 445 model predictions, and provide training data for future refinements, while helping ensure statistically representative 446 characterisation of heterogeneous rock masses.

447 Secondly, imaging hyperspectral sensors can also be deployed on tripod, crewed, and uncrewed aircraft to remotely capture 448~1 to 10 cm resolution data over large areas of exposed rock. This resolution is comparable to the scale of laboratory tests for 449 physical and mechanical properties, but with a large spatial extent that could enable detailed rock-mass characterisation, 450 through the integration of remotely estimated physical and mechanical property estimates, remotely mapped fracture 451 information (e.g., Dewez et al., 2016; Thiele et al., 2017), and numerical simulation techniques (e.g., Cundall et al., 2008; 452 Ivars et al., 2007).

453 Finally, we caution that further development and the acquisition of a larger, more diverse training database is undoubtedly 454 needed before this approach can be confidently applied to industrial applications, especially for outcrop mapping. The 455 lower-quality of hyperspectral data acquired outside of laboratory conditions and the variety of weathering processes that can 456 influence outcrop surfaces, require approaches that are robust and carefully validated. However the required sensors and 457 acquisition techniques already exist, suggesting cm-scale mapping of outcrop physical and mechanical properties is 458 achievable, with appropriate site-specific calibration and validation.

4596 Conclusions

460 Our machine learning models demonstrate that hyperspectral data can be used as a proxy for the physical and mechanical 461 properties in the sampled andesitic and basaltic volcanic rocks, with cross validated R2 scores of 0.7 to 0.8. Physical 462 properties, mechanical behaviour, and reflection spectra are influenced by a complex combination of primary and secondary 463 (alteration or weathering) mineralogy, glass content, porosity, grain size, and surface roughness. Disentangling the influence 464 of these properties on spectral reflectance (for complex mixtures; i.e. rocks) remains challenging but our findings 465 demonstrated that machine learning techniques can be used to find informative relationships between spectral and physical 466 and mechanical properties. Further work is required to assess how robust these predictions are, and if they can be generalised 467 or are best applied after site-specific training. We are confident that our results (and other recent work by e.g., Bakun-Mazor 468 et al., 2024; Kereszturi et al., 2023) underpin how hyperspectral data can serve as informative and easy-to-acquire proxy for 469 physical and mechanical properties of volcanic rocks.

470

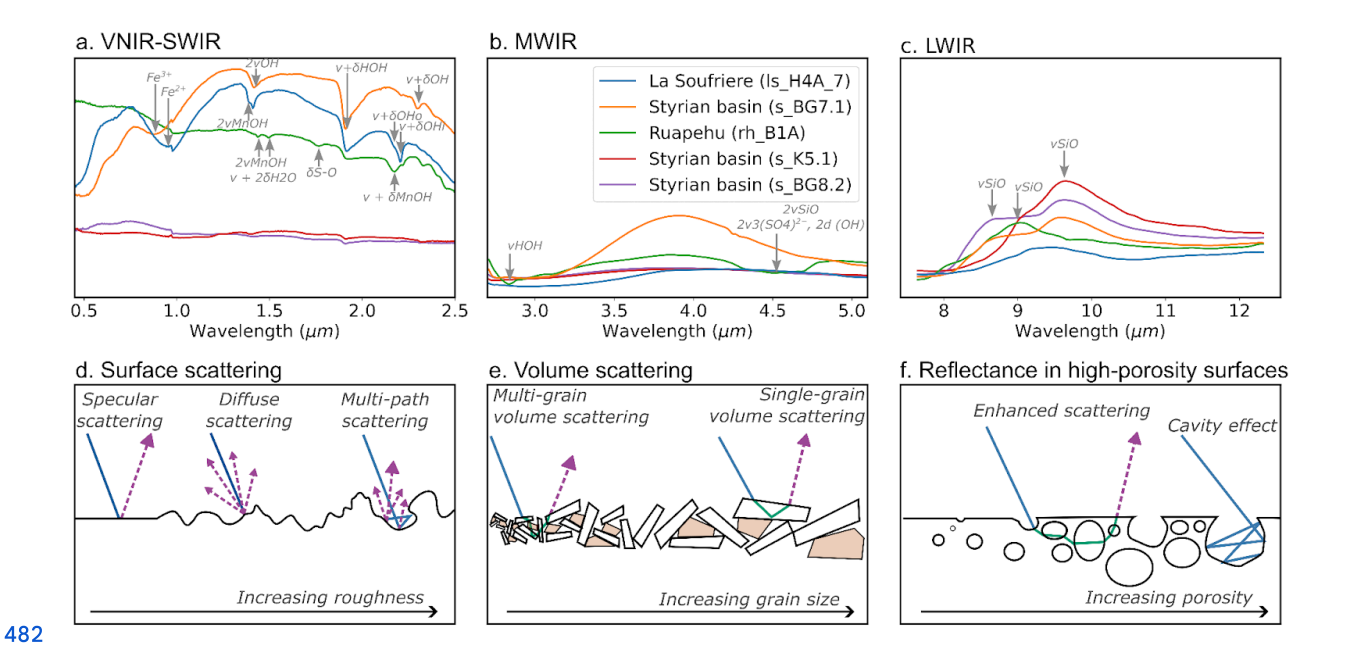
471 Table 1: Spectral indices used to spectrally characterize our samples. Absorption features are classified according to the notation 472 of Laukamp et al., (2021), denoting stretching-related absorptions with v and bending-related absorptions with v and were 473 quantified by fitting an asymmetric gaussian to the specified spectral range and recording its amplitude as a measure of 474 absorption depth. This fitting was conducted using hylite (Thiele et al., 2021), and included a hull correction step to remove 475 spectral features broader than the target range.

Short name	Target	Spectral range (nm)	Indicator for	
$\rm H_2O$	$vOH+\delta H_2O$	1800–2120	Molecular water in e.g., clay minerals.	
ОН	vOH	1350–1600	Hydroxyl groups in clay minerals and hydroxylated sulfates (kaolinite, alunite, illite, etc).	

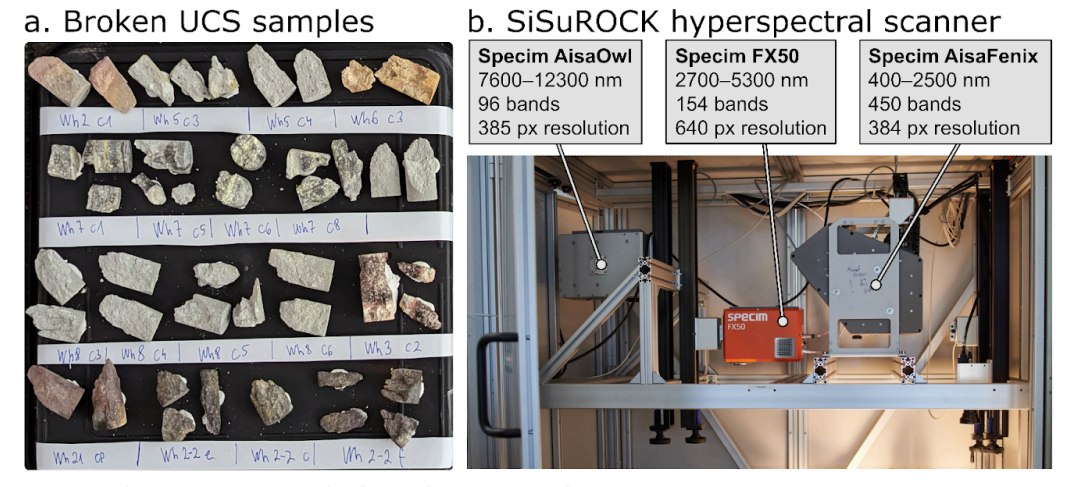
Al-OH	$v + \delta(Al)$ -OH	2150–2240	Hydroxyl groups in Al-rich phyllosilicate minerals including illite, smectite, kaolinite, etc.		
Mg-OH	$v + \delta(Mg)OH$	2280–2330	Hydroxyl groups in Mg-bearing phyllosilicate, like Mg-rich smectites (e.g., hectorite).		
SO_4	δSO	1700–1800	Indicator for the presence of sulfate-bearing minerals, including gypsum and alunite.		
Silica	vSiO	4400–4600	Indicator for quartz or amorphous silica via the second overtone SiO absorption. This was used (rather than the LWIR feature) to avoid interference with plagioclase.		
Kaolinite	v + δM2OHo	2100–2200	Depth of the $v + \delta(Al)$ -OH related doublet typical of kaolinite group minerals. Note that the hull correction applied prior to fitting removes the influence of the deeper absorption at 2200 nm.		

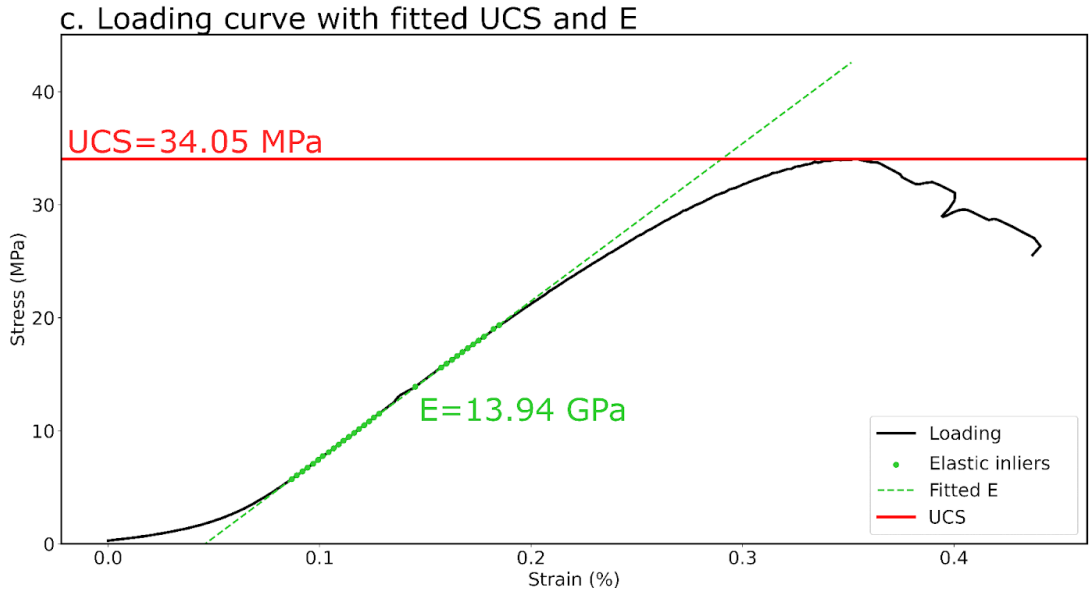
477 Table 2: Five-fold cross validated R2 scores for the machine learning approaches trained and tested on: (1) basaltic (MFI < 0.4), (2) 478 andesitic (MFI > 0.4), and (3) combined subsets. The best R2 scores for each property are indicated in bold. The ensemble models 479 were constructed by combining the best-performing SVR and MLP models.

	Lasso	PLSR	SVR	MLP (uni)	MLP (multi)	Ensemble
Density	0.39	0.51	0.76	0.82	0.85	0.84
Density (basalt) Density (andesite)	0.5 0.32	0.47 0.47	0.77 0.79	0.75 0.85	0.83 0.83	0.78 0.84
Porosity	0.33	0.48	0.74	0.79	0.81	0.81
Porosity (basalt) Porosity (andesite)	0.39 0.31	0.49 0.49	0.77 0.74	0.73 0.80	0.81 0.77	0.76 0.80
UCS	0.21	0.18	0.59	0.69	0.66	0.67
UCS (basalt) UCS (andesite)	0.56 0.1	<0 <0	0.76 0.57	0.76 0.67	0.75 0.67	0.75 0.66
E	0.30	0.36	0.65	0.67	0.67	0.70
E (basalt) E (andesite)	0.44 0.31	0.41 0.41	0.68 0.64	0.73 0.62	0.75 0.62	0.73 0.65

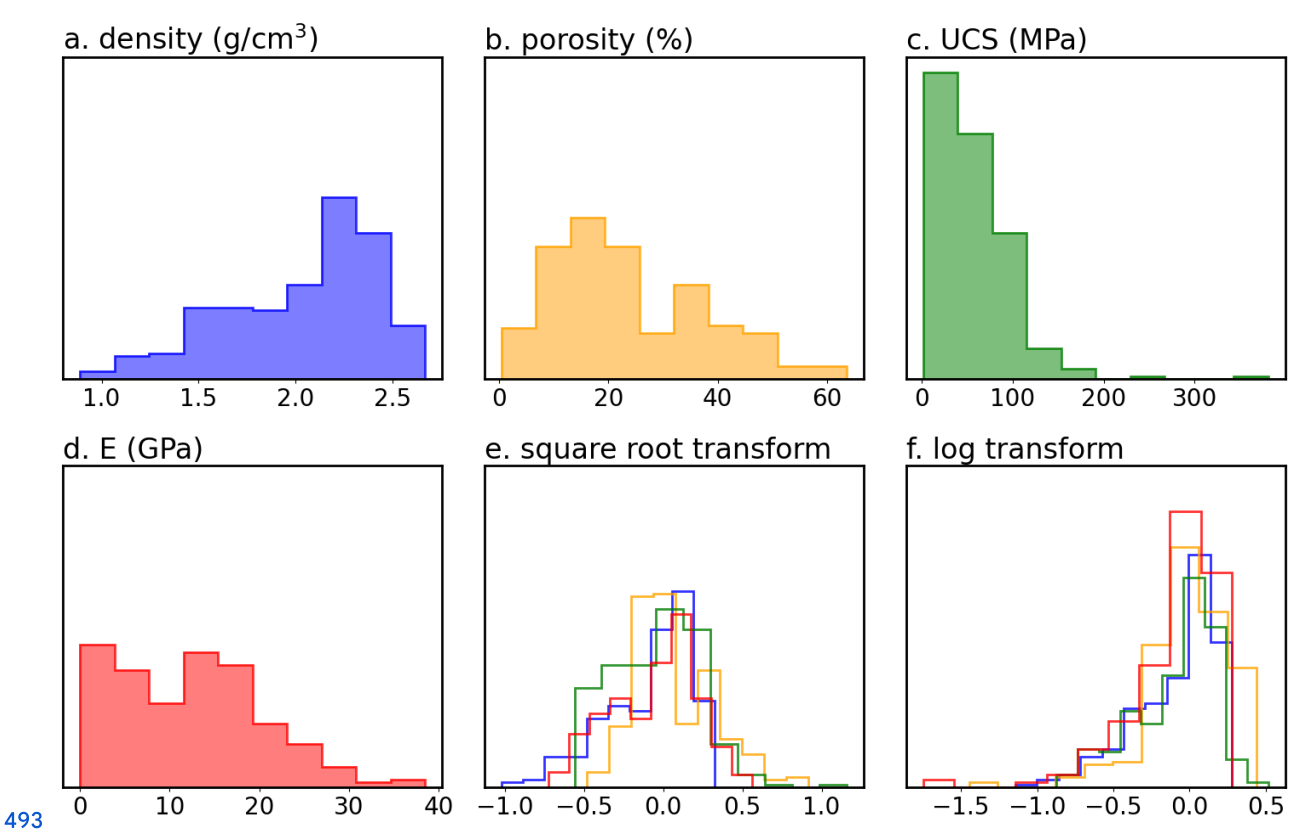


483 Figure. 1: Mineralogical and physical controls on hyperspectral reflectance spectra. Examples of absorption features caused by 484 minerals commonly found in volcanic rocks are shown for the VNIR-SWIR (a), MWIR (b) and LWIR (c) ranges, as described in 485 depth by Laukamp et al., (2021). Typical surface (d) and volume scattering (e) interactions are shown, highlighting the effect of 486 increasing surface roughness and grain size. An example of how these processes operate simultaneously, and are both strongly 487 influenced by porosity, is shown in (f). Note that these are all wavelength dependent, especially where the wavelength of light 488 approaches the scale of variation.

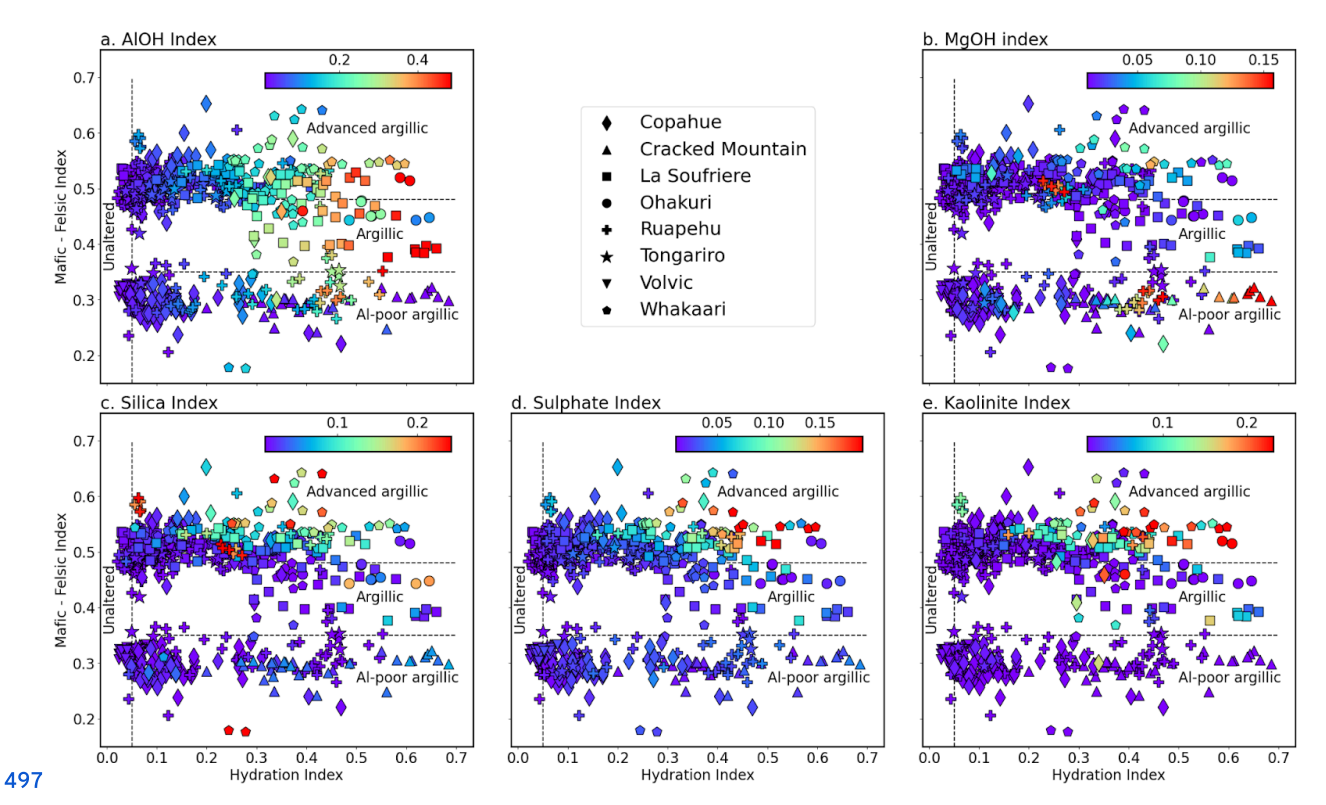




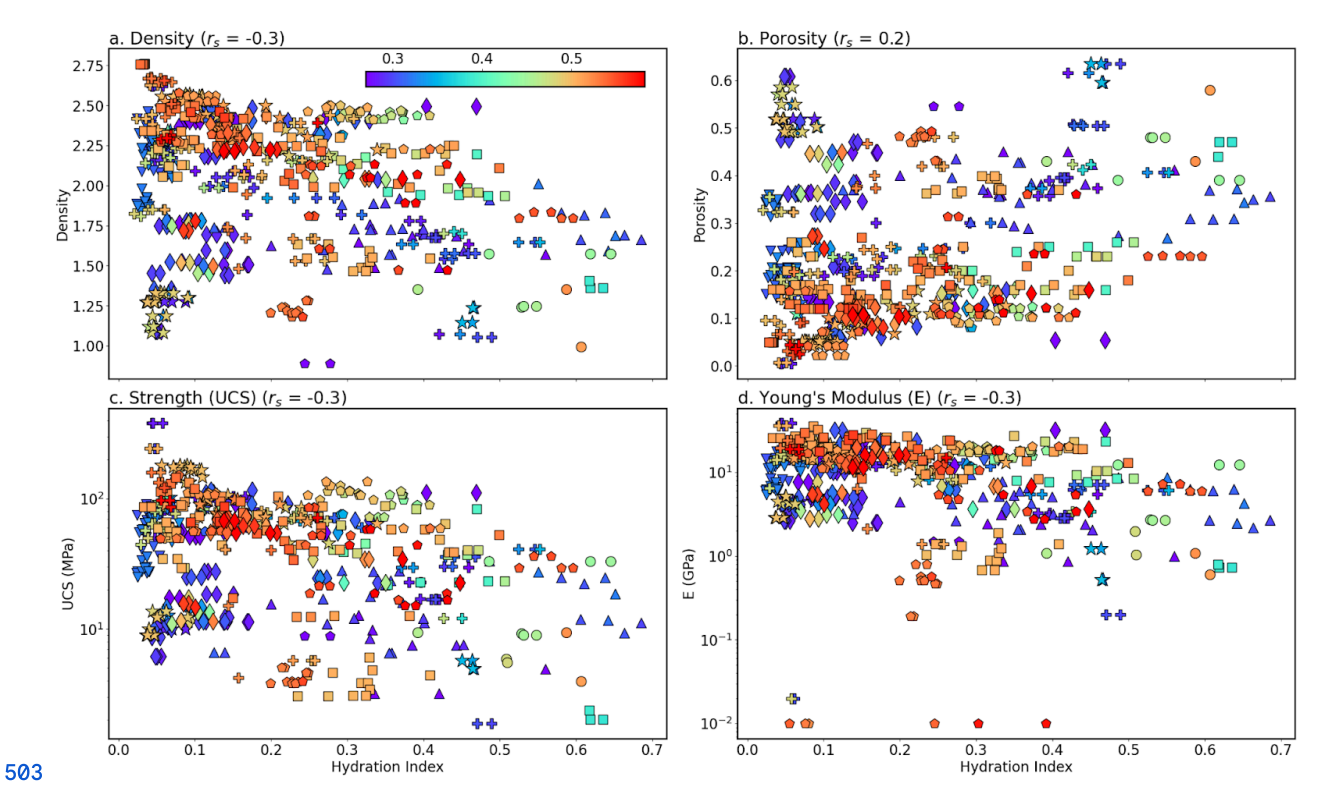
490 Figure. 2: Post-failure uniaxial compressive strength (UCS) test cores (a) prior to scanning in a SiSuROCK hyperspectral drillcore 491 scanner (b). UCS and Young's modulus (E) were extracted from the corresponding stress-strain curves (c) using an automated 492 RANSAC-based procedure, for direct comparison with the (averaged) sample spectra.



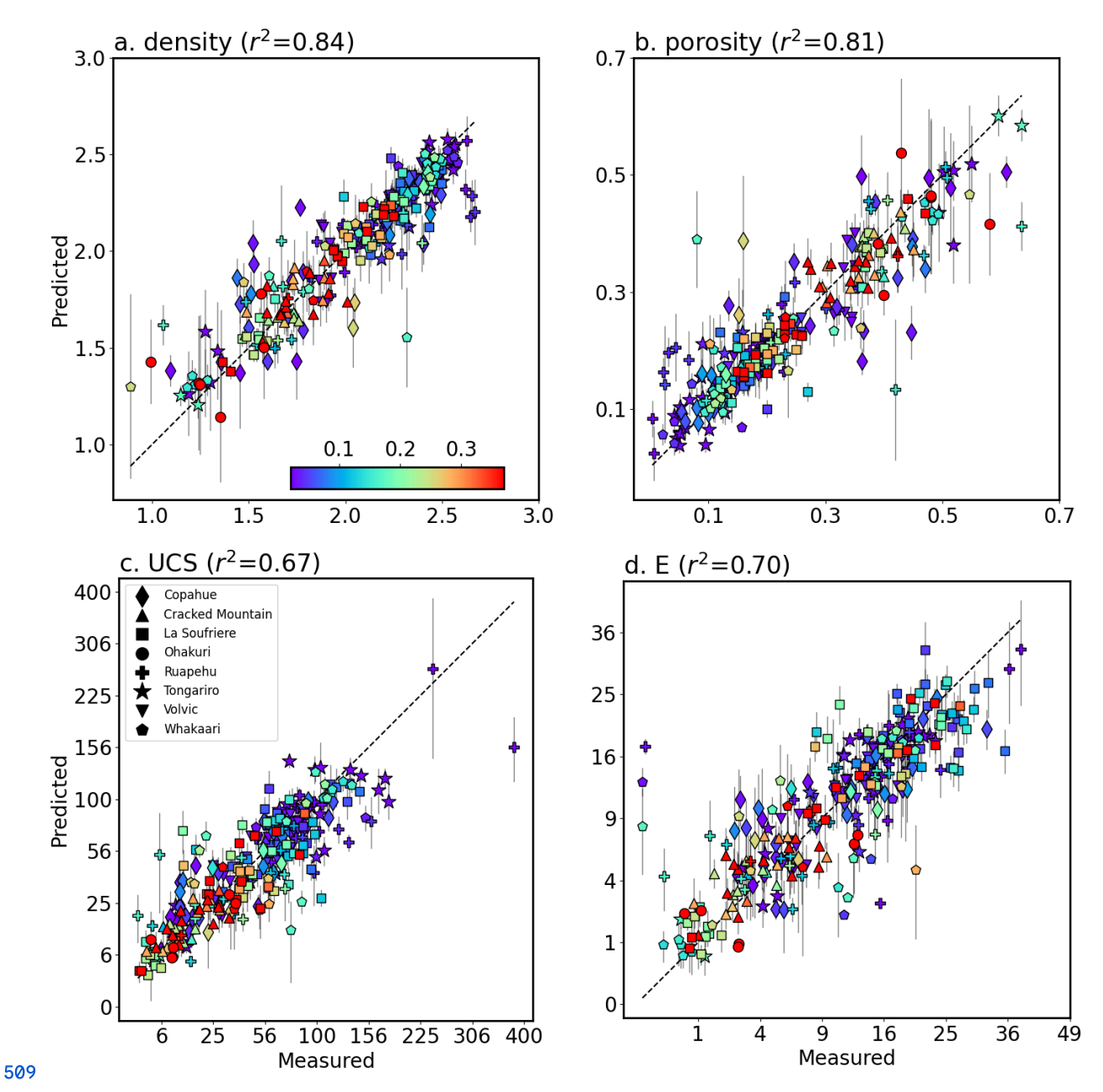
494 Figure. 3: Distributions of the training data before (a-d) and after square root (e) and log (f) transformation. Note that 495 transformed data was normalised to have a median of 0 and 2nd to 98th percentile range of 1. The square root transform (e) 496 resulted in approximately normal distributions.



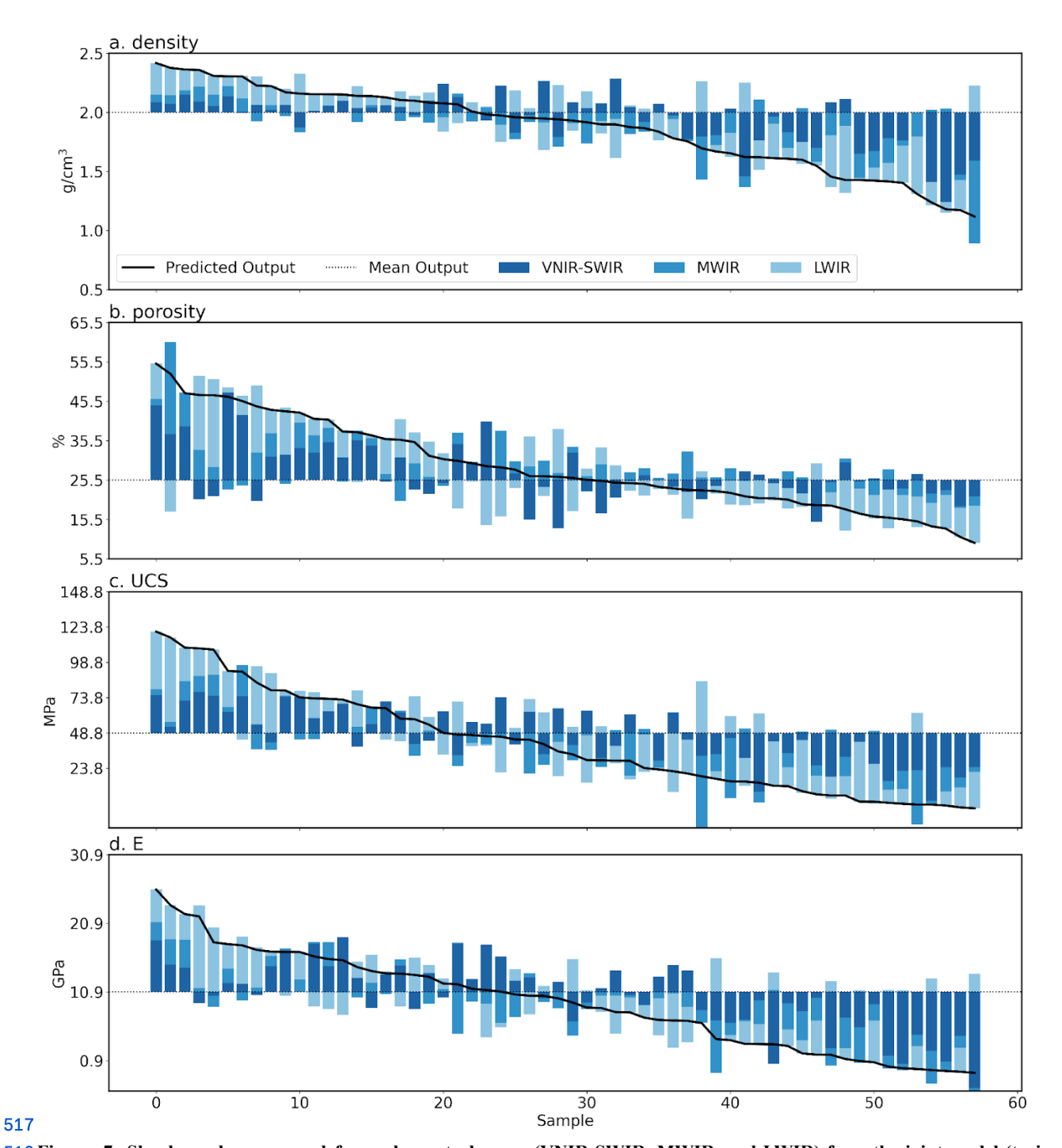
498 Figure. 4: Measured hydration index (x-axis) and Mafic-Felsic Index (MFI; y-axis), coloured by hyperspectral indices for Al-OH 499 bearing phyllosilicates (a), Mg-OH bearing phyllosilicates such as hectorite (b), quartz (c), sulfate (d), and kaolinite (e). The two 500 main clusters indicate the broadly basaltic (lower) or andesitic (upper) composition of the samples, while hydrothermal alteration 501 (and/or surface weathering) results in significant scatter along the x-axis. Distinctive Al-OH and Mg-OH (clay) rich zones indicate 502 argillic alteration, while samples with elevated sulfate and kaolinite indices were likely subject to advanced argillic alteration.



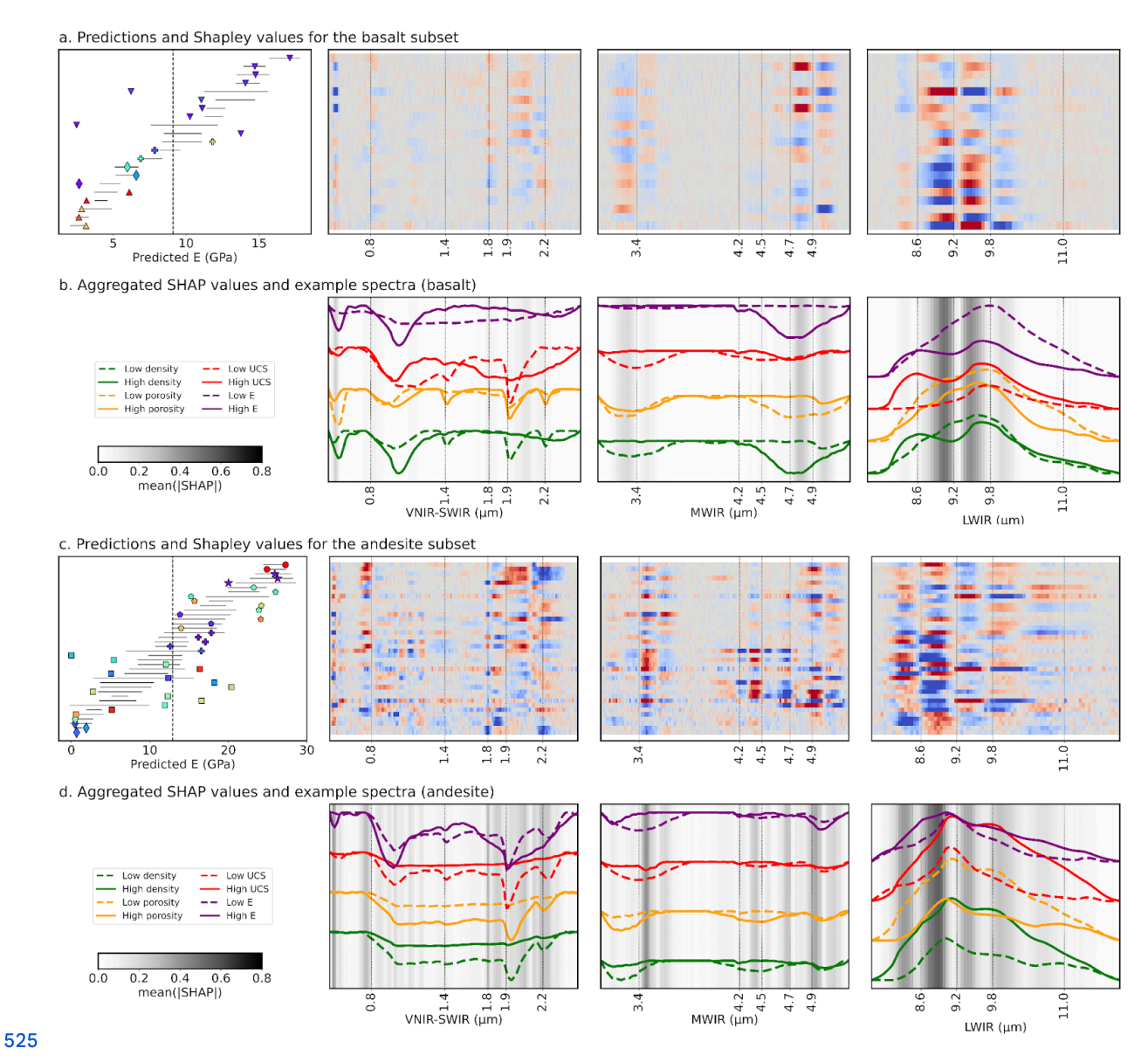
504 Figure. 5: Biplots of our hydration index and density (a), porosity (b), uniaxial compressive strength (UCS) (c) and Young's 505 modulus (E) (d). These indicate that increasing hydration due to hydrothermal alteration and/or weathering tends to decrease 506 density, UCS and E and slightly increase porosity. These trends are (unsurprisingly) quite weak, with Spearman rank correlation 507 coefficients of 0.2–0.3. Colours indicate each sample's MFI, such that basalts are blue and andesites are red. Please refer to the 508 legend of Fig. 3 for the symbols indicating each volcano.



510 Figure. 6: Five-fold cross validation predictions (test-fold predictions for each of the five models) for density (a), porosity (b), 511 uniaxial compressive strength (UCS) (c) and Young's modulus (E) (d) derived using our ensemble of SVM and multilayer 512 perceptron models. The consistency of the ensemble predictions, quantified as the standard deviation of model predictions, are 513 shown as 2σ error bars. The majority of the predictions are thus within error of the measured values, although there are also 514 several notable outliers. Symbols denote the different volcanoes included in the dataset, and colours reflect the hydration index 515 (Fig. 3). Note that the x- and y-axes in (c) and (d) use a square-root scale to better visualise data clustered around lower values of 516 UCS and E.



518 Figure. 7: Shapley values summed for each spectral range (VNIR-SWIR, MWIR, and LWIR) from the joint model (trained on 519 both basalt and andesite) ensemble, indicating the cumulative contribution of each spectral range to predicted density (a), porosity 520 (b), uniaxial compressive strength (UCS) (c) and Young's modulus (E) (d). Values for each property are sorted from high to low 521 predicted value along the x-axis. Higher predictions relative to the mean prediction (dotted line) for density, UCS, and E appear 522 largely driven by LWIR features, while lower values are associated with strong negative contributions from the VNIR-SWIR



526 Figure. 8: Shapley values for our predictions of Young's modulus (E) in the basaltic (a, b) and andesitic (c, d) subsets. These were 527 calculated using the ensemble models trained specifically on each subset (to remove aspects of the joint model focused on 528 lithological distinction). Symbols in the left column indicate the measured property values from each volcano (cf. Fig. 3), while the 529 black solid lines show the (2σ) range of values predicted by the ensemble. Deviations of model predictions from the mean (black 530 dashed line) are the sum of the Shapley values along each row, such that blue values indicate bands that decreased the prediction, 531 while red values indicate bands that increased it. Mean absolute SHAP values (b, d), summarising the sensitivity of the model to 532 specific bands are also shown, with spectra from samples with high (solid) and low (dashed) property values for reference. These 533 Shapley values highlight the correspondence of informative bands and inflection points ("shoulders") in the spectra. Shapley value 534 plots for the other mechanical properties can be found in the supplementary information.

535 Acknowledgements

536 ST and AK were supported by funding from the European Union's Horizon Europe research and innovation programme 537 under grant agreement no 101058483 and from UK Research and Innovation. GK was supported by the Rutherford 538 Discovery Fellowship of the Royal Society of New Zealand - Te Aparangi ("Caught in action - volcano surveillance with 539 hyperspectral remote sensing"; RDF-MAU2003). MH was supported by ANR grant MYGALE ("Modelling the phYsical 540 and chemical Gradients of hydrothermal ALteration for warning systems of flank collapse at Explosive volcanoes"; 541 ANR-21-CE49-0010) and a European Research Council Synergy Grant (ERC-ROTTnROCK-101118491). MH also 542 acknowledges support from the Institut Universitaire de France (IUF). MRC and MT were supported by the TelluS Program 543 of INSU-CNRS ("Edifice structure and rock strength assessment of Copahue volcano (Argentina/Chile): the role of 544 hyperACidic hydrothermal alteration in VolCano stability (AC/VC))". The hyperspectral sensors used for this study were 545 acquired through funding from the Helmholtz Institute Freiberg for Resource Technology, European Regional Development 546 Fund and the Land of Saxony

547 References

- 548 Arens, F., Coco, A., Gottsmann, J., Hickey, J., Kilgour, G., 2022. Multiphysics Modeling of Volcanic Unrest at Mt. Ruapehu
- 549 (New Zealand), Geochem. Geophys. Geosystems 23, e2022GC010572, https://doi.org/10.1029/2022GC010572
- 550 Aubry, T.J., Farquharson, J.I., Rowell, C.R., Watt, S.F.L., Pinel, V., Beckett, F., Fasullo, J., Hopcroft, P.O., Pyle, D.M.,
- 551 Schmidt, A., Sykes, J.S., 2022. Impact of climate change on volcanic processes: current understanding and future
- challenges. Bull. Volcanol. 84, 58. https://doi.org/10.1007/s00445-022-01562-8
- 553 Bakun-Mazor, D., Ben-Ari, Y., Marco, S., Ben-Dor, E., 2024. Predicting Mechanical Properties of Carbonate Rocks Using
- 554 Spectroscopy Across 0.4–12 μm. Rock Mech. Rock Eng. 57, 8951–8968. https://doi.org/10.1007/s00603-024-04035-w
- 555 Chandrasekhar, S. (Subrahmanyan), 1960. Radiative transfer. New York: Dover Publications.
- 556 Cudahy, T., Jones, M., Thomas, M., Laukamp, C., Caccetta, M., Hewson, R., Rodger, A., Verrall, M., 2008. Next generation
- 557 mineral mapping: Queensland airborne HyMap and satellite ASTER surveys 2006–2008. Perth Publicly Available Rep.
- 558 P2007364 152.
- 559 Cundall, P.A., Pierce, M.E., Mas Ivars, D., 2008. Quantifying the size effect of rock mass strength, in: SHIRMS 2008:
- 560 Proceedings of the First Southern Hemisphere International Rock Mechanics Symposium. Australian Centre for
- 561 Geomechanics, pp. 3–15.
- 562 del Potro, R., Hürlimann, M., 2009. A Comparison of Different Indirect Techniques to Evaluate Volcanic Intact Rock
- 563 Strength. Rock Mech. Rock Eng. 42, 931–938. https://doi.org/10.1007/s00603-008-0001-5
- 564 Dewez, T.J.B., Girardeau-Montaut, D., Allanic, C., Rohmer, J., 2016. Facets: a cloudcompare plugin to extract geological
- planes from unstructured 3D point clouds. ISPRS Int. Arch. Photogramm. Remote Sens. Spat. Inf. Sci. XLI-B5, 799.
- 566 https://doi.org/10.5194/isprsarchives-xli-b5-799-2016

- 567 Dincer, I., Acar, A., Cobanoğlu, I., Uras, Y., 2004. Correlation between Schmidt hardness, uniaxial compressive strength and
- 568 Young's modulus for andesites, basalts and tuffs. Bull. Eng. Geol. Environ. 63, 141–148.
- 569 https://doi.org/10.1007/s10064-004-0230-0
- 570 Farquharson, J., Heap, M.J., Varley, N.R., Baud, P., Reuschlé, T., 2015. Permeability and porosity relationships of
- 571 edifice-forming andesites: A combined field and laboratory study. J. Volcanol. Geotherm. Res. 297, 52-68.
- 572 https://doi.org/10.1016/j.jvolgeores.2015.03.016
- 573 Foster, S., Chilton, J., Nijsten, G.-J., Richts, A., 2013. Groundwater—a global focus on the 'local resource.' Curr. Opin.
- 574 Environ. Sustain., Aquatic and marine systems 5, 685–695. https://doi.org/10.1016/j.cosust.2013.10.010
- 575 Franzosi, F., Crippa, C., Derron, M.-H., Jaboyedoff, M., Agliardi, F., 2023. Slope-Scale Remote Mapping of Rock Mass
- 576 Fracturing by Modeling Cooling Trends Derived from Infrared Thermography. Remote Sens. 15, 4525.
- 577 https://doi.org/10.3390/rs15184525
- 578 Griffiths, L., Heap, M.J., Baud, P., Schmittbuhl, J., 2017. Quantification of microcrack characteristics and implications for
- 579 stiffness and strength of granite. Int. J. Rock Mech. Min. Sci. 100, 138–150. https://doi.org/10.1016/j.ijrmms.2017.10.013
- 580 Hapke, B., 2012. Theory of Reflectance and Emittance Spectroscopy. Cambridge University Press.
- 581 Hapke, B., 2008. Bidirectional reflectance spectroscopy: 6. Effects of porosity. Icarus 195, 918–926.
- 582 https://doi.org/10.1016/j.icarus.2008.01.003
- 583 Hapke, B., 2002. Bidirectional Reflectance Spectroscopy: 5. The Coherent Backscatter Opposition Effect and Anisotropic
- 584 Scattering. Icarus 157, 523–534. https://doi.org/10.1006/icar.2002.6853
- 585 Hapke, B., 1993. Theory of Reflectance and Emittance Spectroscopy, Topics in Remote Sensing. Cambridge University
- 586 Press, Cambridge. https://doi.org/10.1017/CBO9780511524998
- 587 Hapke, B., 1986. Bidirectional reflectance spectroscopy: 4. The extinction coefficient and the opposition effect. Icarus 67,
- 588 264–280. https://doi.org/10.1016/0019-1035(86)90108-9
- 589 Hapke, B., 1984. Bidirectional reflectance spectroscopy: 3. Correction for macroscopic roughness. Icarus 59, 41–59.
- 590 https://doi.org/10.1016/0019-1035(84)90054-X
- 591 Hapke, B., 1981. Bidirectional reflectance spectroscopy: 1. Theory. J. Geophys. Res. Solid Earth 86, 3039–3054.
- 592 https://doi.org/10.1029/JB086iB04p03039
- 593 Hardgrove, C.J., Rogers, A.D., Glotch, T.D., Arnold, J.A., 2016. Thermal emission spectroscopy of microcrystalline
- 594 sedimentary phases: Effects of natural surface roughness on spectral feature shape. J. Geophys. Res. Planets 121,
- 595 542–555. https://doi.org/10.1002/2015JE004919
- 596 Harnett, C.E., Heap, M.J., 2021. Mechanical and topographic factors influencing lava dome growth and collapse. J.
- 597 Volcanol. Geotherm. Res. 420, 107398. https://doi.org/10.1016/j.jvolgeores.2021.107398
- 598 Harnett, C.E., Kendrick, J.E., Lamur, A., Thomas, M.E., Stinton, A., Wallace, P.A., Utley, J.E.P., Murphy, W., Neuberg, J.,
- 599 Lavallée, Y., 2019. Evolution of Mechanical Properties of Lava Dome Rocks Across the 1995–2010 Eruption of
- 600 Soufrière Hills Volcano, Montserrat. Front. Earth Sci. 7. https://doi.org/10.3389/feart.2019.00007

- 601 Heap, M.J., Baumann, T., Gilg, H.A., Kolzenburg, S., Ryan, A.G., Villeneuve, M., Russell, J.K., Kennedy, L.A.,
- 602 Rosas-Carbajal, M., Clynne, M.A., 2021a. Hydrothermal alteration can result in pore pressurization and volcano
- 603 instability. Geology 49, 1348–1352. https://doi.org/10.1130/G49063.1
- 604 Heap, M.J., Baumann, T.S., Rosas-Carbajal, M., Komorowski, J.-C., Gilg, H.A., Villeneuve, M., Moretti, R., Baud, P.,
- 605 Carbillet, L., Harnett, C., Reuschlé, T., 2021b. Alteration-Induced Volcano Instability at La Soufrière de Guadeloupe
- 606 (Eastern Caribbean). J. Geophys. Res. Solid Earth 126, e2021JB022514. https://doi.org/10.1029/2021JB022514
- 607 Heap, M.J., Gravley, D.M., Kennedy, B.M., Gilg, H.A., Bertolett, E., Barker, S.L.L., 2020a. Quantifying the role of
- 608 hydrothermal alteration in creating geothermal and epithermal mineral resources: The Ohakuri ignimbrite (Taupō
- 609 Volcanic Zone, New Zealand). J. Volcanol. Geotherm. Res. 390, 106703.
- 610 https://doi.org/10.1016/j.jvolgeores.2019.106703
- 611 Heap, M.J., Troll, V.R., Harris, C., Gilg, H.A., Moretti, R., Rosas-Carbajal, M., Komorowski, J.-C., Baud, P., 2022.
- Whole-rock oxygen isotope ratios as a proxy for the strength and stiffness of hydrothermally altered volcanic rocks. Bull.
- 613 Volcanol. 84, 74. https://doi.org/10.1007/s00445-022-01588-y
- 614 Heap, M.J., Villeneuve, M., Albino, F., Farquharson, J.I., Brothelande, E., Amelung, F., Got, J.-L., Baud, P., 2020b. Towards
- 615 more realistic values of elastic moduli for volcano modelling. J. Volcanol. Geotherm. Res. 390, 106684.
- 616 https://doi.org/10.1016/j.jvolgeores.2019.106684
- 617 Heap, M.J., Violay, M.E.S., 2021. The mechanical behaviour and failure modes of volcanic rocks: a review. Bull. Volcanol.
- 618 83, 33. https://doi.org/10.1007/s00445-021-01447-2
- 619 Hickey, J., Pascal, K., Head, M., Gottsmann, J., Fournier, N., Hreinsdottir, S., Syers, R., 2022. Magma pressurization
- sustains ongoing eruptive episode at dome-building Soufrière Hills volcano, Montserrat. Geology 50, 1261–1265.
- 621 https://doi.org/10.1130/G50239.1
- 622 Hoek, E., Diederichs, M.S., 2006. Empirical estimation of rock mass modulus. Int. J. Rock Mech. Min. Sci. 43, 203–215.
- 623 Huang, J., Liu, S., Liu, W., Zhang, C., Li, S., Yu, M., Wu, L., 2021. Experimental Study on the Thermal Infrared Spectral
- Variation of Fractured Rock. Remote Sens. 13, 1191. https://doi.org/10.3390/rs13061191
- 625 Hunt, G.R., Vincent, R.K., 1968. The behavior of spectral features in the infrared emission from particulate surfaces of
- 626 various grain sizes. J. Geophys. Res. 1896-1977 73, 6039–6046. https://doi.org/10.1029/JB073i018p06039
- 627 Ivars, D.M., Deisman, N., Pierce, M., Fairhurst, C., 2007. The synthetic rock mass approach-a step forward in the
- characterization of jointed rock masses, in: 11th ISRM Congress. OnePetro.
- 629 Kamath, A.V., Thiele, S.T., Kirsch, M., Gloaguen, R., 2025. Multiphysics property prediction from hyperspectral drill core
- data. Solid Earth, 16(4/5), 351-365. https://doi.org/10.5194/se-16-351-2025
- 631 Kereszturi, G., Heap, M., Schaefer, L.N., Darmawan, H., Deegan, F.M., Kennedy, B., Komorowski, J.-C., Mead, S.,
- Rosas-Carbajal, M., Ryan, A., Troll, V.R., Villeneuve, M., Walter, T.R., 2023. Porosity, strength, and alteration Towards
- a new volcano stability assessment tool using VNIR-SWIR reflectance spectroscopy. Earth Planet. Sci. Lett. 602, 117929.
- 634 https://doi.org/10.1016/j.epsl.2022.117929

- 635 Kereszturi, G., Schaefer, L.N., Miller, C., Mead, S., 2020. Hydrothermal Alteration on Composite Volcanoes: Mineralogy,
- 636 Hyperspectral Imaging, and Aeromagnetic Study of Mt Ruapehu, New Zealand. Geochem. Geophys. Geosystems 21,
- 637 e2020GC009270. https://doi.org/10.1029/2020GC009270
- 638 Kidd, M., Kereszturi, G., Kennedy, B., Heap, M., Procter, J., 2025. Linking hydrothermal alteration to rock mechanics:
- comparative analysis of andesitic volcanoes in Aotearoa New Zealand.
- 640 Kirkland, L.E., Herr, K.C., Adams, P.M., 2003. Infrared stealthy surfaces: Why TES and THEMIS may miss some
- substantial mineral deposits on Mars and implications for remote sensing of planetary surfaces. J. Geophys. Res. Planets
- 642 108. https://doi.org/10.1029/2003JE002105
- 643 Kirkland, L.E., Herr, K.C., Salisbury, J.W., 2001. Thermal infrared spectral band detection limits for unidentified surface
- materials. Appl. Opt. 40, 4852–4862. https://doi.org/10.1364/AO.40.004852
- 645 Laukamp, C., Cudahy, T., Cleverley, J.S., Oliver, N.H.S., Hewson, R., 2011. Airborne hyperspectral imaging of
- 646 hydrothermal alteration zones in granitoids of the Eastern Fold Belt, Mount Isa Inlier, Australia. Geochem. Explor.
- 647 Environ, Anal. 11, 3–24. https://doi.org/10.1144/1467-7873/09-231
- 648 Laukamp, C., Rodger, A., LeGras, M., Lampinen, H., Lau, I.C., Pejcic, B., Stromberg, J., Francis, N., Ramanaidou, E., 2021.
- 649 Mineral Physicochemistry Underlying Feature-Based Extraction of Mineral Abundance and Composition from
- 650 Shortwave, Mid and Thermal Infrared Reflectance Spectra. Minerals 11, 347. https://doi.org/10.3390/min11040347
- 651 Lee, J., Cook, O.J., Argüelles, A.P., Mehmani, Y., 2023. Imaging geomechanical properties of shales with infrared light. Fuel
- 652 334, 126467. https://doi.org/10.1016/j.fuel.2022.126467
- 653 Leight, C.J., Ytsma, C., McCanta, M.C., Dyar, M.D., Glotch, T.D., 2024. Compositional Characterization of Glassy Volcanic
- 654 Material From VSWIR and MIR Spectra Using Partial Least Squares Regression Models. Earth Space Sci. 11,
- 655 e2023EA003439. https://doi.org/10.1029/2023EA003439
- 656 Leiter, S., Russell, J.K., Heap, M.J., Barendregt, R.W., Wilson, S., Edwards, B., 2024. Distribution, intensity, and timing of
- 657 palagonitization in glaciovolcanic deposits, Cracked Mountain volcano, Canada. Bull. Volcanol. 86, 32.
- 658 https://doi.org/10.1007/s00445-024-01724-w
- 659 Lewicka, E., Guzik, K., Galos, K., 2021. On the Possibilities of Critical Raw Materials Production from the EU's Primary
- 660 Sources. Resources 10, 50. https://doi.org/10.3390/resources10050050
- 661 Loche, M., Scaringi, G., Blahůt, J., Melis, M.T., Funedda, A., Da Pelo, S., Erbì, I., Deiana, G., Meloni, M.A., Cocco, F.,
- 662 2021. An Infrared Thermography Approach to Evaluate the Strength of a Rock Cliff. Remote Sens. 13, 1265.
- 663 https://doi.org/10.3390/rs13071265
- 664 Lund, J.W., Toth, A.N., 2021. Direct utilization of geothermal energy 2020 worldwide review. Geothermics 90, 101915.
- 665 https://doi.org/10.1016/j.geothermics.2020.101915
- 666 Lundberg, S., Lee, S.-I., 2017. A Unified Approach to Interpreting Model Predictions.
- 667 https://doi.org/10.48550/arXiv.1705.07874

- 668 Lyon, R.J.P., 1965. Analysis of rocks by spectral infrared emission (8 to 25 microns). Econ. Geol. 60, 715-736.
- 669 https://doi.org/10.2113/gsecongeo.60.4.715
- 670 Mineo, S., Pappalardo, G., 2016. The Use of Infrared Thermography for Porosity Assessment of Intact Rock. Rock Mech.
- 671 Rock Eng. 49, 3027–3039. https://doi.org/10.1007/s00603-016-0992-2
- 672 Mordensky, S.P., Villeneuve, M.C., Farquharson, J.I., Kennedy, B.M., Heap, M.J., Gravley, D.M., 2018. Rock mass
- properties and edifice strength data from Pinnacle Ridge, Mt. Ruapehu, New Zealand. J. Volcanol. Geotherm. Res. 367,
- 674 46–62. https://doi.org/10.1016/j.jvolgeores.2018.09.012
- 675 Mustard, J.F., Hays, J.E., 1997. Effects of Hyperfine Particles on Reflectance Spectra from 0.3 to 25 μm. Icarus 125,
- 676 145–163. https://doi.org/10.1006/icar.1996.5583
- 677 Osterloo, M.M., Hamilton, V.E., Anderson, F.S., 2012. A laboratory study of the effects of roughness on the thermal infrared
- 678 spectra of rock surfaces. Icarus 220, 404–426. https://doi.org/10.1016/j.icarus.2012.04.020
- 679 Poganj, A., Heap, M.J., Baud, P., 2025. Spatial distribution of alteration and strength in a lava dome: Implications for
- large-scale volcano stability modelling. J. Volcanol. Geotherm. Res.
- 681 Pola, A., Crosta, G., Fusi, N., Barberini, V., Norini, G., 2012. Influence of alteration on physical properties of volcanic rocks.
- Tectonophysics 566–567, 67–86. https://doi.org/10.1016/j.tecto.2012.07.017
- 683 Portela, B., Sepp, M.D., van Ruitenbeek, F.J.A., Hecker, C., Dilles, J.H., 2021. Using hyperspectral imagery for
- 684 identification of pyrophyllite-muscovite intergrowths and alunite in the shallow epithermal environment of the Yerington
- 685 porphyry copper district. Ore Geol. Rev. 131, 104012. https://doi.org/10.1016/j.oregeorev.2021.104012
- 686 Rost, E., Hecker, C., Schodlok, M.C., Van der Meer, F.D., 2018. Rock Sample Surface Preparation Influences Thermal
- 687 Infrared Spectra. Minerals 8, 475. https://doi.org/10.3390/min8110475
- 688 Salisbury, J.W., Eastes, J.W., 1985. The effect of particle size and porosity on spectral contrast in the mid-infrared. Icarus 64,
- 689 586–588. https://doi.org/10.1016/0019-1035(85)90078-8
- 690 Salisbury, J.W., Wald, A., 1992. The role of volume scattering in reducing spectral contrast of reststrahlen bands in spectra of
- 691 powdered minerals. Icarus 96, 121–128. https://doi.org/10.1016/0019-1035(92)90009-V
- 692 Schaefer, L.N., Kereszturi, G., Kennedy, B.M., Villeneuve, M., 2023. Characterizing lithological, weathering, and
- 693 hydrothermal alteration influences on volcanic rock properties via spectroscopy and laboratory testing: a case study of
- 694 Mount Ruapehu volcano, New Zealand. Bull. Volcanol. 85, 43. https://doi.org/10.1007/s00445-023-01657-w
- 695 Schaefer, L.N., Kereszturi, G., Villeneuve, M., Kennedy, B., 2021. Determining physical and mechanical volcanic rock
- 696 properties via reflectance spectroscopy. J. Volcanol. Geotherm. Res. 420, 107393.
- 697 https://doi.org/10.1016/j.jvolgeores.2021.107393
- 698 Schodlok, M.C., Whitbourn, L., Huntington, J., Mason, P., Green, A., Berman, M., Coward, D., Connor, P., Wright, W.,
- 699 Jolivet, M., Martinez, R., 2016. HyLogger-3, a visible to shortwave and thermal infrared reflectance spectrometer system
- 700 for drill core logging: functional description. Aust. J. Earth Sci.

- 701 Shapley, L.S., 1973. On Balanced Games without Side Payments, in: Hu, T.C., Robinson, S.M. (Eds.), Mathematical
- 702 Programming. Academic Press, pp. 261–290. https://doi.org/10.1016/B978-0-12-358350-5.50012-9
- 703 Simpson, M.P., Rae, A.J., 2018. Short-wave infrared (SWIR) reflectance spectrometric characterisation of clays from
- 704 geothermal systems of the Taupō Volcanic Zone, New Zealand. Geothermics 73, 74–90.
- 705 https://doi.org/10.1016/j.geothermics.2018.01.006
- 706 Soltani, M., Moradi Kashkooli, F., Dehghani-Sanij, A.R., Nokhosteen, A., Ahmadi-Joughi, A., Gharali, K., Mahbaz, S.B.,
- 707 Dusseault, M.B., 2019. A comprehensive review of geothermal energy evolution and development. Int. J. Green Energy
- 708 16, 971–1009. https://doi.org/10.1080/15435075.2019.1650047
- 709 Strehlow, K., Gottsmann, J.H., Rust, A.C., 2015. Poroelastic responses of confined aquifers to subsurface strain and their use
- 710 for volcano monitoring. Solid Earth 6, 1207–1229. https://doi.org/10.5194/se-6-1207-2015
- 711 Swanson, E., Wilson, J., Broome, S., Sussman, A., 2020. The Complicated Link Between Material Properties and
- 712 Microfracture Density for an Underground Explosion in Granite, J. Geophys. Res. Solid Earth 125, e2020JB019894.
- 713 https://doi.org/10.1029/2020JB019894
- 714 Takemura, T., Golshani, A., Oda, M., Suzuki, K., 2003. Preferred orientations of open microcracks in granite and their
- 715 relation with anisotropic elasticity. Int. J. Rock Mech. Min. Sci. 40, 443-454.
- 716 https://doi.org/10.1016/S1365-1609(03)00014-5
- 717 Thiele, S.T., Bnoulkacem, Z., Lorenz, S., Bordenave, A., Menegoni, N., Madriz, Y., Dujoncquoy, E., Gloaguen, R., Kenter,
- 718 J., 2022. Mineralogical Mapping with Accurately Corrected Shortwave Infrared Hyperspectral Data Acquired Obliquely
- 719 from UAVs. Remote Sens. 14, 5. https://doi.org/10.3390/rs14010005
- 720 Thiele, S.T., Grose, L., Samsu, A., Micklethwaite, S., Vollgger, S.A., Cruden, A.R., 2017. Rapid, semi-automatic fracture
- and contact mapping for point clouds, images and geophysical data. Solid Earth 8, 1241.
- 722 Thiele, S.T., Kirsch, M., Lorenz, S., Saffi, H., El Alami, S., Contreras Acosta, I.C., Madriz, Y., Gloaguen, R., 2024.
- 723 Maximising the value of hyperspectral drill core scanning through real-time processing and analysis. Front. Earth Sci. 12.
- 724 https://doi.org/10.3389/feart.2024.1433662
- 725 Thiele, S.T., Lorenz, S., Kirsch, M., Acosta, I.C.C., Tusa, L., Hermann, E., Möckel, R., Gloaguen, R., 2021. Multi-scale,
- 726 multi-sensor data integration for automated 3-D geological mapping using hylite. Ore Geol. Rev. 136.
- 727 https://doi.org/10.1016/j.oregeorev.2021.104252
- 728 Tramontini, M., Rosas-Carbajal, M., Heap, M.J., Besson, P., Marteau, J., García, S., Zyserman, F.I., 2025. The effects of
- 729 hydrothermal alteration in the upper edifice of Copahue volcano (Argentina-Chile). Presented at the IAVCEI Conference,
- 730 Geneva.
- 731 Vairé, E., Heap, M.J., Baud, P., van Wyk de Vries, B., 2024. Quantifying the physical and mechanical heterogeneity of
- 732 porous volcanic rocks from the Chaîne des Puys (Massif Central, France). Bull. Volcanol. 86, 49.
- 733 https://doi.org/10.1007/s00445-024-01742-8

- 734 van der Meer, F., Kopačková, V., Koucká, L., van der Werff, H.M.A., van Ruitenbeek, F.J.A., Bakker, W.H., 2018.
- 735 Wavelength feature mapping as a proxy to mineral chemistry for investigating geologic systems: An example from the
- 736 Rodalquilar epithermal system. Int. J. Appl. Earth Obs. Geoinformation 64, 237–248.
- 737 https://doi.org/10.1016/j.jag.2017.09.008
- 738 Vincent, R.K., Hunt, G.R., 1968. Infrared Reflectance from Mat Surfaces. Appl. Opt. 7, 53-59.
- 739 https://doi.org/10.1364/AO.7.000053
- 740 Vrakas, A., Dong, W., Anagnostou, G., 2018. Elastic deformation modulus for estimating convergence when tunnelling
- through squeezing ground. Géotechnique 68, 713–728. https://doi.org/10.1680/jgeot.17.P.008
- 742 Williams, D.B., Ramsey, M.S., 2024. Infrared spectroscopy of volcanoes: from laboratory to orbital scale. Front. Earth Sci.
- 743 12. https://doi.org/10.3389/feart.2024.1308103
- 744